



TÉCNICO
LISBOA

Degradation analysis of craters on Mars

Magda Sofia Carvoeiras Rocha

Thesis to obtain the Master of Science in

ELECTRICAL AND COMPUTER ENGINEERING

Supervisors:

Prof. Pedro Miguel Berardo Duarte Pina

Prof. Jorge dos Santos Salvador Marques

Examination Committee

Chairperson: Prof. João Fernando Cardoso Sequeira

Supervisor: Prof. Jorge dos Santos Salvador Marques

Members of the Committee: Prof. Jacinto Carlos Marques Peixoto do Nascimento

November 2015

*"I used to live in an Orphanage.
It was dark and cold and lonely.
At night, I looked up at the sparkly sky and felt better.
I dreamed I could fly there.
In America, I can make all my dreams come true...
Thank-you for the "Spirit" and the "Opportunity"."*

-Sofi Collis, the nine-year-old girl who named the Mars rovers

Acknowledgments

I want to dedicate this section to thank my supervisors Professor Jorge Marques and Pedro Pina for their dedication and patience throughout the elaboration of this dissertation.

A special thanks goes out to my brother in law for his contribution in reading the thesis.

This project is the culmination of an important phase of my live, finishing my degree, which would not be possible without the great friendships I made in this institution, so a very special thanks to those who accompanied me on this journey.

I would also like to thank my family for the support they provided me through my entire life and in particular, I must acknowledge my parents for their love and encouragement, my sister for the great example that she is, to my boyfriend for his kindness and my grandmother who will always be my inspiration in life and my biggest fan.

Resumo

O rápido crescimento da tecnologia de aquisição de imagem levou a um enorme aumento na quantidade de imagens captadas por satélites planetários. A possibilidade de analisar o conteúdo dessas imagens foi um ponto de viragem na área de pesquisa planetária.

Imagens de crateras de impacto estão entre as características geomorfológicas planetárias mais estudadas porque fornecem informação acerca de processos geológicos e são uma poderosa ferramenta para estimar a idade das superfícies planetárias. Além disso estudar estas estruturas ajuda a obter informações para uma futura exploração robótica ou mesmo humana ao Planeta Vermelho.

Para superar anos de análise visual, neste projeto é apresentado um método para a classificação automática do grau de preservação (ou de degradação) das crateras de Marte com base no estado do seu rebordo. O rebordo de uma cratera é a elevação de terreno em torno da linha de contorno da cratera, e foi escolhida devido ao seu padrão diferenciado ao longo das fases de evolução desta.

Características de textura foram extraídas e o desempenho do classificador testado em crateras de diferentes tamanhos e formas localizadas em 2 distintos quadrantes de Marte, Lunae Palus e Syrtis Major. O método proposto levou a desempenhos de classificação de ~ 80%.

Embora o algoritmo de classificação seja menos adequado para classificar crateras de pequenas dimensões,(raio inferior a 16 pixels) e crateras com um GT demasiado ambiguo que causou dúvidas ao estabelecer a categoria correta para cada seção. Fenómenos de sobreposição de crateras e com iluminações solares muito distintas revelou-se outro obstáculo no desempenho do classificador, no entanto este estudo, revelou ser uma contribuição importante para a construção futura de catálogos de preservação de crateras com um maior grau de exactidão.

Palavras-chave: Marte, crateras, preservação, rebordo, classificação.

Abstract

The rapid growth of image acquisition technology led to an enormous increase on the amount of planetary images taken by satellites. The possibility of analyzing the content of those images was a turning point on planetary research.

Impact craters are among the most studied geomorphologic planetary features because they yield information about past geological processes and are a powerful tool for estimating the ages of planetary surfaces. Furthermore studying these structures helps to uncover information that can drive future robotic or even human exploration to the Red Planet.

To overcome years of visual analysis, this project presents a method for the automatic classification of the degree of preservation of Mars craters based on the state of its rim. The rim is the raised area around the edge of the crater that was chosen to evaluate the preservation status since it shows a differentiated pattern along the temporal evolution phases of the crater.

Texture features were extracted and the performance of the SVM classifier was tested in craters of different sizes and shapes located on two distinct regions, Mars Lunae Palus and Syrtis Major Quadrangles. The proposed method led to classification accuracies of ~80%.

Although the classification algorithm is less efficient to classify small craters (radius smaller to 16 pixels) and also on those with an “ambiguous” GT that caused doubts on establishing the correct assignment for each section. Phenomena such as overlapping craters and illumination problems caused by the sun's position was also an obstacle to the good performance of the classifier, however this proved to be a good contribution to the future construction of automatic crater catalogs with higher precision.

Keywords: Mars, craters, preservation, rim, classification.

Contents

Acknowledgments	3
Resumo	4
Abstract	5
List of Tables	8
List of Figures	9
Acronyms	11
Chapter 1-Introduction	12
1.1. Motivation	12
1.2. State of the Art	15
1.3. Goals	18
1.4. Thesis Outline	18
Chapter 2-Craters characterization	20
2.1. Methodology	20
2.2. Craters Outline	24
2.2.1 Edge Map	25
2.2.2 Crater Delineation	27
2.3. Feature Extraction	28
2.3.1 Gradient Histograms	34
2.3.2 Gradient Percentiles	35
2.4. Support Vector Machine Classifier	36
2.4.1 One-against-All Classifier	37
2.4.2 RBF Kernel	39

Chapter 3-Experimental Results	
3.1. Introduction	40
3.2. Image DataSets	40
3.3. Ground-truth construction	44
3.4. Evaluation Criteria	45
3.4.1 Cross Validation	45
3.4.2 SVMTRAIN parameters	45
3.4.3 Final Statistics: Confusion Matrix and Final Accuracy	47
3.5. Classifier Results	48
3.5.1 DataSet1 results	48
3.5.1.1 Histogram gradient features results	48
3.5.1.2 Percentile features results	56
3.5.2 DataSet2 results	58
Chapter 4-Conclusions and Future work	64
Bibliography	66
Appendix A Overall implementation of the SVM classifier	68

List of Tables

Table 2.1: Tree Stages of Crater Conservation with the related features [12]	21
Table 3.1: HiRISE images and craters DataSets	41
Table 3.2: Statistic Results for Data Set1 using histogram as feature vectors	48
Table 3.3: Statistic Results for Data Set1 using data percentiles as feature vectors	57
Table 3.4: Two examples where the algorithm fails due to craters small size	59
Table 3.5 Statistic Results for the entire Data Set2 using histogram as feature vectors	60
Table 3.6: Statistic Results for the entire Data Set2 using data percentiles as feature vectors	60
Table 3.7 Statistic Results for part of Data Set2 using histogram as feature vectors	61
Table 3.8: Statistic Results for part of Data Set2 using data percentiles as feature vectors	63

List of Figures

Figure 1.1: Crater density comparison between two distinct planetary surfaces	13
Figure 1.2: Superposition between two craters A and B	13
Figure 1.3: : Examples of simple (A) and complex (B) craters on Mars	14
Figure 2.1: Structure of a simple and complex crater and rim location	22
Figure 2.2: The tree main implementation steps	22
Figure 2.3: On the left the input image (Crater from DataSet1) and on the right the transformed contour.	24
Figure 2.4. Crater of Figure 2.3 in polar coordinates	25
Figure 2.5 Edge map for the crater in Figure 2.3	26
Figure 2.6 Edge map and optimal contour (yellow line) related to the crater in Figure 2.3	28
Figure 2.7: Endurance Crater, roughly 150m in diameter.	29
Figure 1.8: NavCam slope map on the West Spur. blue areas have low overall slope, green areas are moderate, and red areas have high slope.	29
Figure 2.9: Gradient Direction using Sobel Method in the crater of Figure 2.3	31
Figure 2.10: Gradient direction using Sobel Method in the crater of Figure 2.3	31
Figure 2.11: Representation of 5 different preserved craters	32
Figure 2.12: Variation of the dimension of the section ring according to the radius percentage contribution	32
Figure 2.13: Section identification (by numbers and colours)	33
Figure 3.1: Part of the GT for the Data	41
Figure 1.2: Nested Cross Validation for parameters optimization	42

Figure 3.3: Performance examples for SVM classification with features type 1: (left) input image, (center) GT and (right) Algorithm result. ('0' means preserved, '1' moderately preserved/degraded and '2' degraded)	43
Figure 3.4: Crater p002 gradient magnitude histograms	44
Figure 3.5: Crater p003 sections with GT "0"	46
Figure 3.6: Crater p012 sections with GT "0"	50
Figure 3.7: Crater p047 gradient magnitude histograms	51
Figure 3.8: Performance examples for SVM classification with features type 2: (left) input image, (center) GT and (right) Algorithm result. ('0' means preserved, '1' moderately preserved/degraded and '2' degraded)	52
Figure 3.9: The two sections of crater p012 with GT ="0"	52
Figure 3.10 Crater p003 gradient phase histograms	53
Figure 3.11: Feature extraction in case of superposition between two craters	54

List of Acronyms

ANN- Artificial Neural Network

DT- Decision Tree

DP- Dynamic Programming

ESA-European Space Agency

FFT-Fast Fourier Transform

GT- Ground-Truth

HOG- Histogram of Oriented Gradient

MER-Mars Exploration Rover

MRO- Mars Reconnaissance Orbiter

NASA- National Aeronautics and Space Administration

RBF-Radial Basis Function

SVM-Support Vector Machine

Chapter 1-Introduction

1.1. Motivation

The technological advances in satellite sensor area over the past three decades has led to the concept of remote sensing, the primary source of land cover information these days.

By taking long distance images of the surface of the Earth and by extracting information from the pixels combined with supervised classification techniques scientists could gather information, without the physical present of technicians in the field.

Rapidly this concept was expanded to other planets in the Solar System like Mars or the Moon in order to pursue an answer for some of these questions:

- How the frequency of impacts has changed over time.
- How the size of material that has impacted the surfaces of planets has changed over time.
- How important is the evidence of geologic processes that may have modified craters.

Mars is severely bombarded by meteor impacts, mainly because of its thin atmosphere and also because of its close proximity to the *Main Asteroid Belt*, the primary contributor to the number and size of meteors impact that this planet shows. The Red Planet geological structures density, patterns and morphology have always flickered interest among planetary scientists which pursue answers for the dynamics of the planet.

Studies have showed that in an area of one kilometer wide it is possible to see more than 635000 impact craters [1] mainly small impacts, and the real numbers point to 42,000 impact craters with a diameter larger than 5 kilometers [2] or about 385,000 craters larger than 1 km [3] manually identified and catalogued across the entire planet Mars.

Radiometric dating techniques performed in laboratories, by analyzing physical samples of the soil, is an efficient way to date surfaces and that were extremely useful to determine the absolute age of the Moon. These techniques are not possible for Mars and also for other distant bodies, until we can collect samples of the rocks or soils from the surface and analyze them in laboratory.

Nevertheless, the relative age of different surfaces can be estimated by indirect means using geological principles as the calculation of crater densities, or the number of craters of a given diameter per unit area. Larger crater densities is usually an indicator of older surfaces. Figure 1.1 represents a picture from NASA in which region A has a greater crater density indicating it to be older than region B with very few impacts.



Figure 1.1: Crater density comparison between two distinct planetary surfaces

Another method used is the Principle of Superposition, this principle states that a feature on a superficial layer is younger than a feature founded in deeper layer. If a crater is found on the floor of or overlapping the rim of another crater it must be younger. The crater on the bottom must have been there first, making it older. Figure 1.2 represent two craters, B on top of A indicating that B is more recent that A.

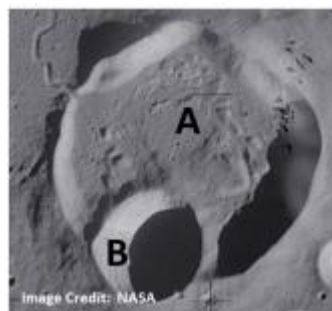


Figure 1.2: Superposition between two craters A and B

The final method is Crater Classification which provides information about the degradation rate of those same craters. The more modified a crater, the older it is. This status can be an additional indicator of obtaining a more precise age of the surface and also to provide useful and detailed information about the geological processes that

have been acting in those regions. Nevertheless, it is important to refer that in these methods can be found some ambiguity, for example if a recent crater occurs near a region with some kind of tectonic movement, there is also a larger probability that its degradation increases at a faster rate, and therefore its individual age estimation would naturally be compromised.

Craters can be distinguished by its morphology in two main groups: Simple or Complex. This classification scheme, which was based on the study of craters exposed by erosion, also seems to apply to the morphology of fresh craters revealed by images of the surfaces of other planets and satellites [2].

On Mars, simple craters are small (typically <6-7 km in diameter) and display a bowl-shaped appearance as showed in Figure 1.3 A. Larger, complex craters ($\geq 6-7$ km diameter) display more complex interior structures, including central rises (central peaks), central rings of peaks (peak rings), central depressions (central pits), and gravity induced wall collapse (wall terraces) like the crater in Figure 1.3 B.

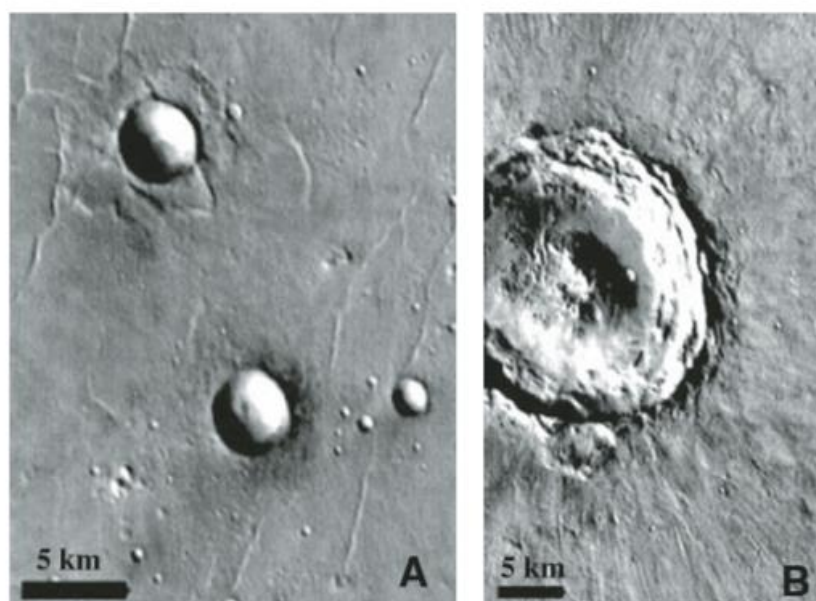


Figure 1.3: Examples of simple (A) and complex (B) craters on Mars

A degradation index, proposed by Ambrose (2006), is one of the first attempts to quantify the degradation (or preservation) shown by impact craters. Although developed for lunar craters and based on qualitative evaluations of the craters and surrounding terrains it opened the way for using objective measures quantifying the degradation of these structures. It also identified that the major degradation factors are due to the subsequent impacts after the crater was formed (new craters), landslides

and ejecta deposition, lava flooding, floor fracturing, crater infilling, glacial accumulation and degassing events, among many others. [4]

However we must have in consideration that Ambrose projected an index for Earth's Moon which as Mercury, lack liquid water on their surfaces that would erode impact craters faster over time and also lack of an atmosphere and tectonic activity. The inexistence of these factors made the surface of these bodies very old when compared with Mars and Earth.

Although there are many different factors modifying the shape and pristine characteristics of a crater after its formation along the vast geological time scale, it is verifiable that there exists a global relationship between these factors and the degradation state of the craters. For example, a fresh looking crater with a low degradation state has been less subject to the erosion factors and for this reason has sharp rims and has low chances of having suffered subsequent impacts from a meteor (it will naturally show a lower degradation index in any built scale). As the age of the crater increases we normally see a change on its morphology, the rim begins to be more rounded and at advanced stages can become hardly noticeable or can be completely erased. The number of overlapping impacts can be higher and the presence of rays and bright ejecta, that is a relevant feature of new impacts, are completely inexistence in craters of this type.

The development of an automatic method to quantify the degradation state of impact craters through the detailed analysis of their rims is currently very well welcome by the Planetary Science community, as it could be a new key to new discoveries into the geological history of Mars and also of other planetary bodies.

1.2. State of the Art

Identifying craters manually for the entire planet Mars was naturally the first way for obtaining a global catalogue. This type of procedure has been attempted by Barlow in 1988, Kuzmin et al. in 1989, Costard in 1989, Rodionova et al. in 2000 and Robbins and Hynes in 2012 [5].

The first complete crater catalog made by visual inspection was, as stated, initially built by Barlow (1988) [6] and consisted of 42 284 craters identified on the entire Martian surface. The most recent version of the Martian crater's database was built by Robbins and Hynes (2012) [6] and includes 384 343 craters extracted from high-resolution images of the *Thermal Emission Imaging System's* camera.

Due to the increasing number of craters unveiled by the increasing resolution of image sensors aboard the planetary probes, the use of automated procedures for the detection of craters naturally emerged. Crater Detection Algorithm techniques were explored like circle fitting, highlight and shadow region matching, template matching object-oriented method, texture analysis, and machine learning.

Circle fitting was used by Cheng et al. in 2003 [7] that apply it to automated navigation over extraterrestrial small bodies, by Magee et al. in 2003 that showed results using edge processing and template matching, by Kim and Muller in 2003 [7] that have applied texture analysis and ellipse fitting on the Digital Terrain Model (DTM) and optical images and by Sawabe et al. in 2006 [7]. that have used multiple boundary based approaches and combined the results obtained to enhance the adaptive ability to differentiate crater sizes. Those approaches include classifying images considering illumination, finding edge pixels of interest using a vectorized feature extractor and the usage of Hilditch's [7] thinning algorithm and Hough transform in addition to the previous methods .

All of the described approaches proposed by Sawabe et al (2006) [7] could not properly detect elliptical shapes of impact craters.

Highlight and shadow region matching techniques were used by Urbach and Stepinski (2009) [8] which based their theory on characteristic shapes of craters making possible for small craters to be detected. Their detection percentage is about 70% what is not rather enough.

Bandeira et al. (2007) [9] developed an impact crater recognition on Mars procedure based on a probability volume created by template matching. The procedure has mainly 3 phases: candidate selection, template matching and crater detection. In a pre-processing phase, the areas that correspond to crater rims are identified in a gray level image, though the majority of the noise in the image is eliminated. A template matching procedure is applied to the binary images of these regions, using the Fast Fourier Transform, and finally, a probability volume model is calculated to determine the location and dimension of the impact craters present in an image. The approach reached a crater recognition rate of 86.57% and achieved a false detection rate of 15.95%, in average.

Object-oriented method developed by Yue et al. (2008) [10], used objects segmented from images based on size, shape and color features in order to enable the distinction between targets.

Barata et al. (2004) [11] employed texture analysis for crater detection, measuring the variance in each tile and using shadows, high local variance, to detect craters.

However, the results presented were not satisfactory, since the false positive rate was revealed too high.

Machine learning methods have also been applied to recognize and catalog impact craters. Wetzler et al. in 2005 [12] have used bagging and AdaBoost with feedforward neural networks as base learners, support vector machines (SVM), and continuously scalable template models to originate crater detectors from ground-truthed images. Support Vector Machine had revealed a better performance on crater detection compared to boundary-based approaches such as Hough Transform. The problem lies on the need of vast ground-truth data and computational resource since SVM models they developed involve nearly five thousand support vectors. Burl proposed the use of blocked FFT implementation on SVM decision function to decrease the computational demands.

To achieve high level of accuracy investigators have tried to combine more than one technique. Honda et al. (2000) combined machine learning approaches with boundary based methods [13]. Kim et al. (2005) [13] plan three step system to crater detection. In the first stage, they eliminate noise in the image, in the second stage of the algorithm, primitive arcs are organized by graph and conic section fitting. Finally the possible craters are verified using a false crater classifier based on artificial neural networks.

However, all of these Crater Detection Algorithms, assume that all detected craters are circular and only provide as output the radius and location of each one. The local evaluation of the craters rims, like degradation or preservation status is very useful to, for instance, analyze past climates on Mars. The proper identification of where the irregularities along the contour really are, can give an important contribution to the extraction of the features around that area and consequently allowing the enrichment of crater catalogs with the real contour of each crater and its degree of degradation.

Two preliminary approaches have been attempted on this subject, one based on a sequence to find and link the crater edges in polar coordinates (Marques and Pina, 2013) and the other based on watershed transform and other mathematical morphology operators (Pina and Marques, 2013). These were exploratory approaches that were not capable of generalization in dealing with large datasets and also revealing to be too sensitive to local image texture variations.

Persuading this goal, Marques and Pina (2015) [14] developed an improved and more robust algorithm that is actually capable of delineate with high precision the contour of the craters achieving 95% of correct delineations in a representative dataset of the Martian craters, with more than 1000 annotated craters.

This algorithm has two main steps, the first one is the definition of an Edge Map in polar coordinates and the second is the delineation of the crater itself using Dynamic Programming.

1.3. Goals

The main goal of this master thesis is the development of an automatic method for the characterization of impact crater rims that can be used as a basis for a degradation index in order to translate their current preservation conditions into quantitative and meaningful information.

The work involved the use of an algorithm [11] developed to thoroughly extract the outline of the crater by means of Dynamic programming. This has allowed a correct definition of the border.

The second step involves a proper extraction of the features around that same area adjusting the region of the extraction to the size of the crater. Those features measured the data distribution by means of histograms and percentiles vectors.

The last stage involved the construction of a classifier that uses the features extracted from the images into the learning/training process of the classifier, those were previously assign to a label (ground-truth) related to their degree of conservation with the help of knowledge's of investigator Pedro Pina.

A Mars surface images annotated database of 170 images taken by HiRISE camera was used for the development of the programming code, using as tool the MATLAB, version R2014a.

The choice of using MATLAB as programming software has primarily to do with its toolbox function that is easy to use making the code shorter and more intuitive and also because of the visual results.

1.4. Thesis Outline

The work is organized in 4 main chapters, being the first one the introduction where previous developed work and the delineation of the main goals are discussed.

The second chapter describes the methodology proposed and the algorithms developed to delineate the rim of each crater and to extract the image features of the

rim as well as the classifiers selected for the automatic classification of the degradation state of the craters.

The third chapter concerns the experimental part of this work. It starts by describing the type and dataset of Martian images used, makes a preliminary description of the features extracted that are used as input for the training and test sets of the SVM, and the criteria used for the classification of the crater sections into ternary labels. Experimental results are also analyzed and discussed.

The final chapter approaches the global conclusions of the developed work in addition to possible future improvements.

Chapter 2-Craters characterization

2.1. Methodology

The study of impact craters opens a window to Research Institutes and Space Agencies like NASA to finally have a better understanding of the history and geology of Mars. After the crater formation procedure, observing the outputs of the erosion processes tells us a lot about that surface age.

The first naïve approach would be to arrange a group of experts and give them the task of analyzing those images and to come up with a final classification for each one of them. Nevertheless the amount of resources needed is enough to completely discard the idea.

This thesis aims to overcome this difficulty and reach an automatic preservation (or degradation) index for the craters.

Three preservation degrees will be considered as suggested by Prof. Pedro Pina: Preserved, Modified and Degraded. Several questions must be addressed: What distinguishes them? Which characteristics are different from crater image to crater image? Shown below is a data Table with illustrative features that distinguish the tree degree of crater conservation.

Stage I-Preserved Craters	
<ul style="list-style-type: none"> • Near perfect craters; • Raised Rims; • Can sometimes see ejecta blanket, central peak or ray ejecta; • Look fresh. 	
Stage II- Modified Craters	

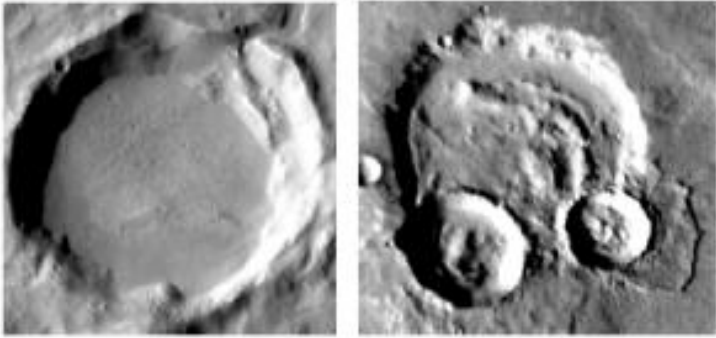
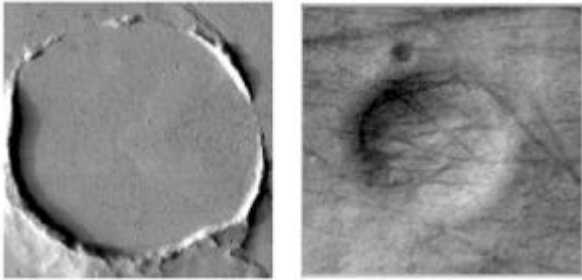
<ul style="list-style-type: none"> • Middle-age craters with evidence of modification; • Rim may appear uneven or somewhat irregular in shape; • Craters may have smooth floor (partially filled in with sediments); • Can range from being slightly to severely modified. 	
Stage III- Destroyed Craters	
<ul style="list-style-type: none"> • Oldest Craters that have been severely altered; • Broken Rims; • Craters have been filled in almost completely by sediments; • Flat appearance and very worn away. 	

Table 2.1: Tree Stages of Crater Conservation with the related features

The rim was the feature chosen by two main reasons: its appearance evolves over time by erosion and has distinguishing characteristics in each one of the tree conservation stages: Preserved, Modified and Destroyed and the fact that is always present, contrary to the other characteristics of a crater (as for example central peaks).

The strategy was to use the state of the rim as his sharpness and relief to classify the crater image into one of the tree considered stages.

The rim identified in Figure 2.1 is not only the outline of the crater but also all the region part that extends above the height of the local surface, caused by debris ejected while the crater is being formed. Degraded craters have diminished rims, which reduce rim's flank and rim's height and when compared with the more recent ones have considerable less definition. The more recent ones have normally more pronounced and sharp rims around the whole contour and with less discontinuities.

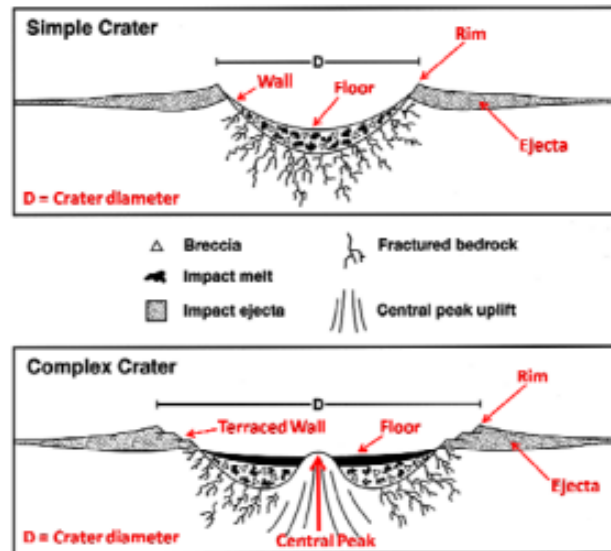


Figure 2.1: Structure of a simple and complex crater and rim location

The implementation phases to characterize a crater image were the following:



Figure 2.2: The tree main implementation steps

The first step was to detect the crater outline so the entire rim region could be analyzed.

The *Dynamic Programming* algorithm (explained more ahead) delineated the contour of the craters using as input the Edge Map. It allowed to properly identify the crater in the input image.

This algorithm was used because of its robustness in delineating a wide variety of craters in different images.

In the second stage the features were extracted only in the rim region using for that the coordinates of the outline returned by the algorithm used in step one.

While analyzing other alternatives to the rim the crater depth and filling was a possibility it could be measured by the number of bright pixels in the image that is considerably larger when compared with a ghost/destroyed crater. This technique is

being used nowadays by astronomical software that can look for patterns of brightness change to distinguish celestial objects like planets and stars.

One possible strategy to follow in the future is to use a group of classification techniques that allows to identify in a given range the intensity of the presence of the different features and combined the results.

The third and final stage represent the accomplishment of classification for each section of the craters. The use of a ternary label representing each stage of preservation was assigned to all the Data Base images and it is denoted as GT (Ground Truth). The GT information is used in the training phase of the SVM (Support Vector Machine) classifier. To the Fresh/Preserved Craters was assigned the label zero, to Modified craters the label 1 and to Destroyed craters with label 2.

SVM is a supervised classification method that performs classification by finding the hyperplane that maximizes the margin between the two classes.

The SVM can efficiently perform a non-linear classification using what is called the kernel trick, mapping their inputs into high-dimensional feature spaces.

Other classification algorithms as DT (Decision Trees), ANN (Artificial Neural Networks), KNN (k-nearest neighbor classification) and Bayesian classification could have been an alternative to the use of SVM.

The DT handle multi-output problems however it can generate highly complex algorithms that lead frequently to overfitting.

ANN [15] are perceived to be difficult to apply successfully. It is difficult to select the type of network architecture, the initial values of parameters such as learning rate and momentum, the number of iterations required to train the network and the choice of initial weights.

K-Nearest Neighbor (KNN) [16] is another approach that is easy to implement, with high degree of efficacy in many classification tasks in many classification domains. However, when the amount of training data is large, k-nearest neighbor approach becomes computationally intensive and its classification accuracy could be drastically degraded when the number of attributes raises.

Bayesian approach due to its simplicity and low computational cost in both the training and classifying stage has been commonly implemented in different types of domains and applications. However, this generative method has been reported to be less accurate than discriminative methods such as SVM as proved by Godbole [17] in 2006 while studding different types of classification method in her Ph. D. thesis.

The decision was to use SVM since it has revealed good results in other related problems of supervised digital image classification. For the ternary classification procedure used on this work the solution was to decompose the multiclass problem

into three binary class problems, using one-versus-all approach, in which the classifier with the highest output function assigns the class.

The main problem while implementing an automated method of classification like this happens when the rules that define each category are ambiguous or if it exists some characteristics in the image that leads the classifiers to interpret something as being the crater rim when in reality is not. Those difficulties were caused by shadows in the surface caused by the sun's position and crater superposition leading to the analysis of a different crater that covered the one being examined.

2.2. Craters Outline

The first step aims to delineate the crater rim as represented in Figure 2.3.

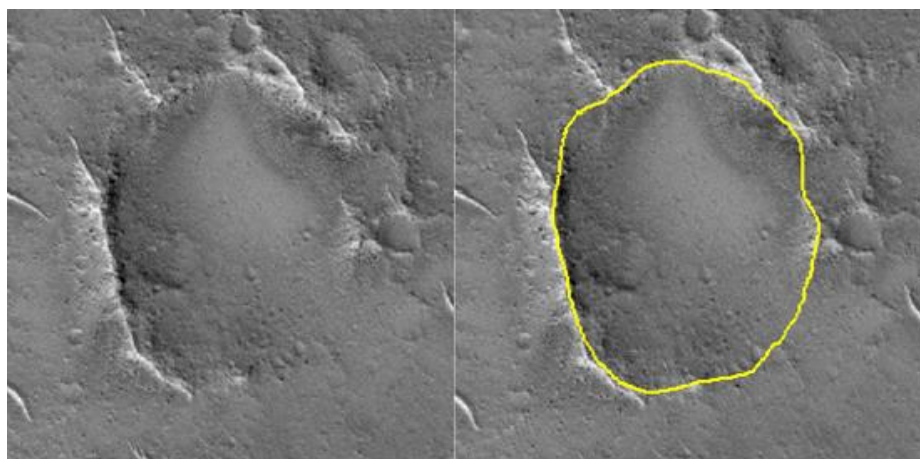


Figure 2.3: On the left the input image (Crater from DataSet1) and on the right the transformed contour in Cartesian coordinates

The algorithm used in this thesis was proposed in [14] and it will be briefly summarized. In the first stage, the algorithm detects intensity transactions in the image of the crater and finally links all the edges in order to design the contour.

Edge detection algorithms such as Sobel, Canny, Prewitt and Roberts fail to extract the contour because when detecting potential edge points the algorithms were not able to make the distinction between terrain irregularities and parts of the contour.

Therefore, the algorithm proposed uses an Edge Map $e(x) \in [0,1]$, measures the directional variation of intensity on each point and assigns the value $e(x) = 0$ to a pixel when there is a strong intensity variation in the neighborhood of x in a orthogonal

direction to the crater contour. The value $e(x) = 1$, is assigned to a pixel if the image is constant in that direction, which means that x is not a part of the contour.

The final stage involves the computation of a closed contour, $x(s)$ which minimizes the energy functional

$$E(x) = \int e(x(s)) ds + E_{\text{int}}. \quad (1)$$

The parameter $E_{\text{int}}(x)$ measures the deviations of the crater contour, $x(s)$, to a circle and s is the arc length parameter of the curve.

2.2.1 Edge Map

As the crater image has an approximately circular shape and the center and the radius are known the original image expressed in cartesian coordinates is converted into polar coordinates. Figure 2.4 shows the plot done to the same crater of Figure 2.3 but this time in polar coordinates. Some previous computations were necessary, like the center coordinates (C_x, C_y) of the crater that were calculated using the average point of the image in horizontal and vertical directions.



Figure 2.4. Crater of Figure 2.3 in polar coordinates

Then the equations were applied to each single pixel of the image

$$x = Cx + (r \times \cos \theta), \quad (2)$$

$$y = Cy + (r \times \sin \theta). \quad (3)$$

where r is the distance of the pixel (x,y) to the crater center and θ is the angle with respect to the xx axis.

A potential edge was associated with large transitions along radial lines, containing the center .The radial intensity is measured by computing the radial gradient

$$g(r, \theta) = |P(r, \theta) * h(r)|. \quad (4)$$

The notation, $P(r, \theta)$ is the input image in polar coordinates, and $h(r)$ is the impulse response of a high pass filter,

$$h(r) = -u(r - T) + 2u(r) - u(r + T), \quad (5)$$

where $u(r)$ is the unit step function. The convolution operation is done along each radial direction.

The edge map is computed using the function

$$e(r, \theta) = \frac{2}{1 + e^{sg(r,\theta)}}, \quad (6)$$

where s is a scalar. The Figure 2.5 reflects the plot of the computed edge map. In this way gradient intensity is mapped into a confidence edge between $[0 \ 1[$.

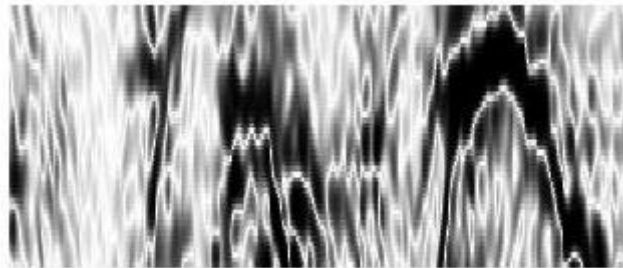


Figure 2.5 Edge map for the crater in Figure 2.3

The crater's radius is known, so the parameter r must be in an interval $[R_{min} \ R_{m\acute{a}x}]$, where R_{min} equals $0.8 \cdot R$ and $R_{m\acute{a}x}$ equals $1.2 \cdot R$.

2.2.2 Crater Delineation

The final and optimal contour, in Figure 2.6, is obtained by the minimization of the energy function. To simplify the problem, we assume that the crater contour is defined in polar coordinates and discretized i.e., we consider N radial directions and discretize the distance to the origin into one of M possible values. Therefore, the contour is defined by a sequence of pairs $(\theta_1, r_1), \dots, (\theta_N, r_N)$ where $\theta_p = 2\pi p/N$ is the angle of the p -th radial direction and r_p the distance of the p -th contour point to the center of the crater. We further assume that $r_p \in \{1, \dots, M\}$. We also discretize the edge map and approximate it by a matrix $e(p, r)$ where $p \in \{1, \dots, N\}, r \in \{1, \dots, M\}$ N is the number of columns of the edge map and M the lines.

We wish to find the sequence r that minimizes the energy functional

$$E(r) = e(1, r_1 = k) + \sum_{p=2}^N e(p, r_p) + c(r_{p-1}, r_p). \quad (7)$$

Dynamic programming is used to minimize the energy functional, under the constraint $r_1 = r_N = k$, where $k \in \{1, \dots, M\}$. The algorithm is repeated for all possible values of $k \in \{1, \dots, M\}$ and the one value that is chosen is the one that minimizes the energy functional. This is done in two phases, the first one is the computation of the optimal costs to go from column 1 and row k to column t and row j , $E_t(j)$. To impose smooth transitions the algorithm assures that the module of transition from r_{p-1} to r_p is less or equal to 1 and the cost associated with that is defined as the branch function

$$c(r_{p-1}, r_p) = \begin{cases} 0 & \text{if } |r_{p-1} - r_p| = 0 \\ \alpha & \text{if } |r_{p-1} - r_p| = 1 \\ +\infty & \text{otherwise} \end{cases} \quad (8)$$

The optimal cost is computed in a forward recursion,

$$E_1(j) = \begin{cases} e(1, k) & \text{if } j = k \\ +\infty & \text{otherwise} \end{cases} \quad (9)$$

$$E_t(j) = e(t, j) + \min_i [E_{t-1}(i) + c(i, j)], t = 2, \dots, N, j = 1, \dots, M. \quad (10)$$

To recover the optimal path, the value of i that minimizes $[E_{t-1}(i) + c(i, j)]$ is stored in a $1 \times N$ size array

$$\psi_t(j) = \underset{i}{\operatorname{argmin}} [E_{t-1}(i) + c(i, j)], t = 2, \dots, N. \quad (11)$$

Backward Recursion is applied to obtain the optimal path $r^* = (r_1^*, r_2^*, \dots, r_N^*)$ using the steps below,

$$r_N^* = k, \quad (12)$$

$$r_{t-1}^* = \psi_t(r_t^*) \quad t = N, \dots, 2. \quad (13)$$

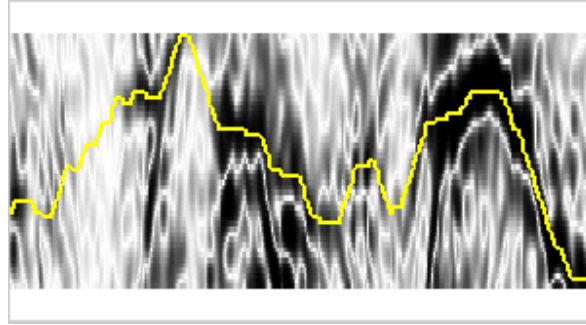


Figure 2.6: Edge map and optimal contour (yellow line) in polar coordinates related to the crater in Figure 2.3

2.3. Feature Extraction

The rim was the feature considered more distinctive to characterize the degree of preservation of the crater and the decision about what kind of features would lead to a better classification results was made based on a bunch of factors.

Features based on surface geometry, texture and color were the possibilities analyzed.

Surface geometry information is useful for distinguishing for example different terrains with geometric characteristics. This kind of feature would be perfect to analyze two classes like rock and sand. A method to distinguish this two would be by features related to its slope, photographed by the two rovers in Mars.

Both Spirit and Opportunity [18] encountered moderate slopes early in their missions, but slopes did not become the forcing function for mobility until Opportunity reached Endurance Crater (Figure 2.7).



Figure 2.7: Endurance Crater, roughly 150m in diameter

Scientists computed the surface normal and after the slope was computed from the normal at each pixel, resulting in a slope map.

Like slope maps, solar energy maps are viewed as color overlays on the original image. Figure 2.8 shows several slope and solar energy maps used for drive planning with Spirit.

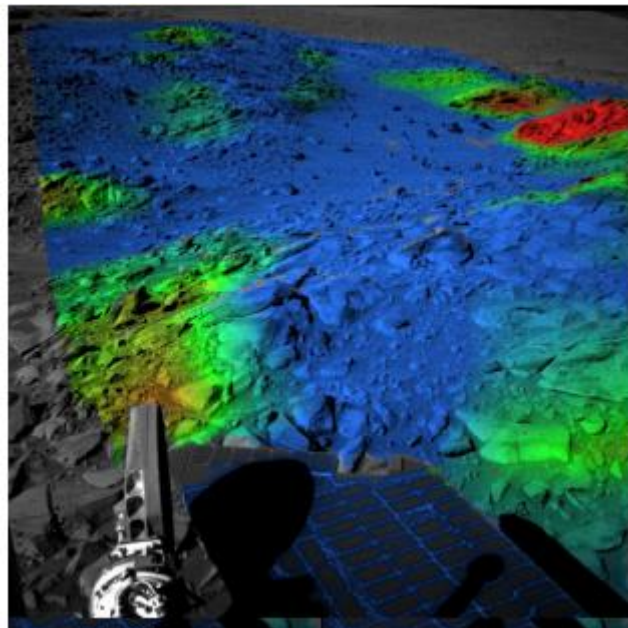


Figure 2.8: NavCam slope map on the West Spur. Blue areas have low overall slope, green areas are moderate, and red areas have high slope.

While sand normally never has a slope greater than its angle of repose predominantly parallel to the ground plane, rock areas project from the ground plane with certain angle. This information could be extracted around the rim of the crater and would give us information about the projection of the rim above the surface. As the images being analyzed are 2D images we are not taking into account the vertical information.

Color features were not appropriate features to use in this case of study.

Color [19] is an obvious distinguishing characteristic of many terrain types however color variation is somehow limited for the surface of Mars. Mars lacks vegetation and this leads to a narrow distribution of colors for distinct terrain types. The color of the region of the crater would not be very distinctive to attribute a relative age to the surfaces however the sediments inside the rim could give information about the terrain, for example, yellowish color sediments indicates moderately solid material lies at or close to the surface and blue tints and softened, blanketed features suggest thick coatings of dust and fine sand. Once again the construction of this feature vector would make sense in color images and not in grayscale images like the ones being study.

Texture features revealed to be the ideal to proper reflect the state of the rim.

Visual texture contains variations of intensities, which form certain repeated patterns. Those patterns can be caused by physical surface properties, such as roughness, or they could result from reflectance differences, such as the color on a surface [20]. Some of the most used texture features are: Gray Level Co-Occurrence Matrix (GLCM), Gabor Textural Feature, Local Binary Pattern (LBP), Wavelet transform and Gradient Histograms. Gradient histograms, the directional in particular, had already proved to be effective in the texture image retrieval, especially in case of the non-homogenous textures. For that reason, to measure the texture of the craters rim, gradient information was extracted across the images.

The gradient of an image has two kinds of information, one is the magnitude (Figure 2.9) and the other is the direction (Figure 2.10) of the gradient. Magnitude gives the information of how rapidly the image is changing and direction of the gradient tells which image direction is changing more rapidly.

For an image intensity function $f(x,y)$, the gradient of function f at coordinates (x,y) is defined as the two dimensional column vector

$$\nabla f = \begin{pmatrix} G_x \\ G_y \end{pmatrix} = \begin{pmatrix} \frac{\partial f}{\partial x} \\ \frac{\partial f}{\partial y} \end{pmatrix}, \quad (14)$$

The component $\frac{\partial f}{\partial x}$ is the gradient in the x direction and $\frac{\partial f}{\partial y}$ is the gradient in y direction.

We can detect the edges in image by computing the magnitude of the vector

$$\|\nabla f\| = \sqrt{G_x^2 + G_y^2}, \quad (15)$$

The direction of gradient can be computed as

$$\alpha(x, y) = \tan^{-1} \left(\frac{G_x}{G_y} \right), \quad (16)$$

where the angle is measured with respect to x-axis and the edge direction at (x, y) is perpendicular to the direction of the gradient vector at the point.

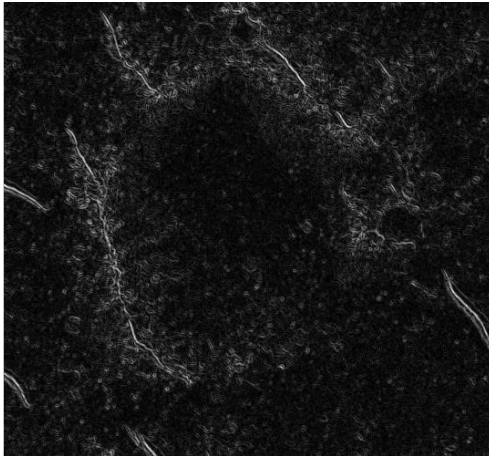


Figure 2.9: Gradient Magnitude using Sobel Method in the crater of Figure 2.3

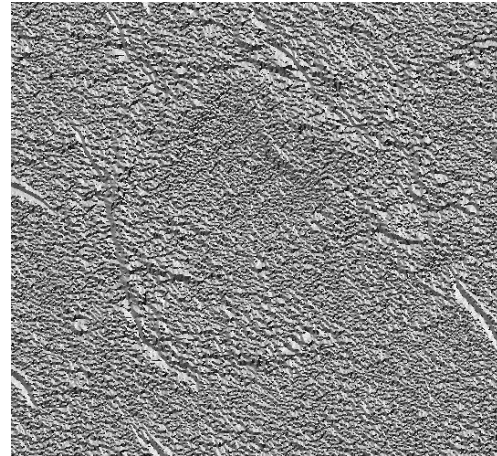


Figure 2.10: Gradient direction using Sobel Method in the crater of Figure 2.3

The Matlab function *atan2* was used instead of *atan* (*arctangent*) function because the *atan2* function gathers information on the signs of G_x and G_y returning the right quadrant of the computed angle, the resulting angle of both function returns different results since $-\frac{\pi}{2} \leq atan \leq \frac{\pi}{2}$ and $-\pi \leq atan2 \leq \pi$.

As the purpose is to analyze the texture in rims region would not make sense to use features of the whole image.

The rim was divided into 8 sections, the features were extracted for each sector and then the classification was obtained for each individual sector.

The idea of dividing the crater into sections and analyzing them as a combo of the behavior on each one seemed the best approach to overcome some ambiguous behavior on the global appearance of the rim. In Figure 2.11 the 3 types of craters stages are represented where in Figure a 5 preserved craters are all different as well as its rims that show distinct inconsistencies around the contour. Some have raised rims all around, others have rims with irregularities with the presence of shadows, ray systems and ejecta blanket. All these characteristics can be present in the same crater's rim or not be present at all. If in a preserved crater a small part of its contour vanishes or if it shows a considerable amount of shadows the crater obviously continues being a preserved crater. The idea was to minimize the errors in the classification by not providing a label by a global analysis for each type of crater. The

classification procedure returns the preservation stage for each section allowing identifying different stages of preservation within the same crater.

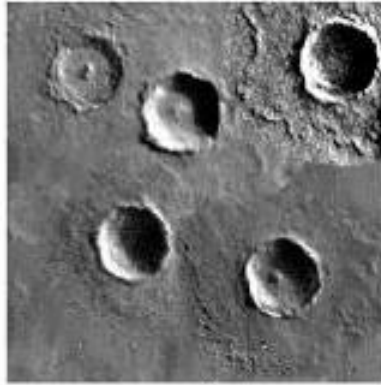


Figure 2.11: Representation of 5 different preserved craters

As seen in Figure 2.12, the distance to the outline that was tested were between 2% and 10% the value of the radius, and incremented by 1% in each iteration.

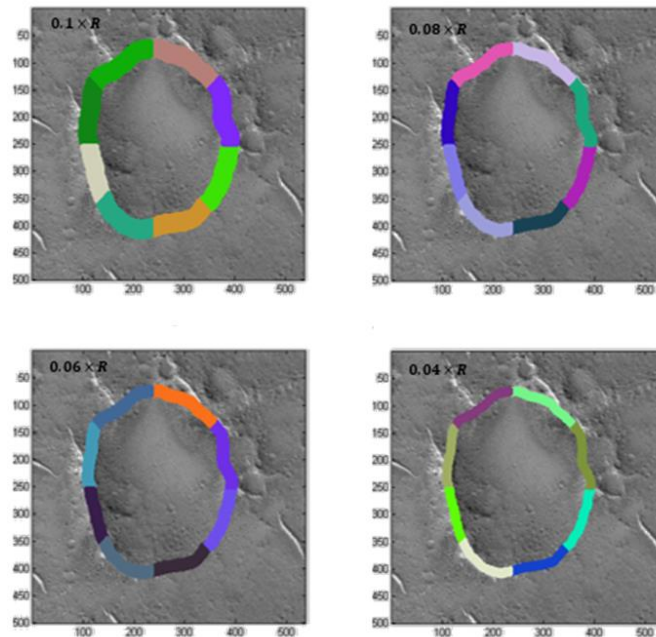


Figure 2.12: Variation of the dimension of the section ring according to the radius percentage contribution

The procedure implemented to select the pixels that met that condition was to store both x and y coordinates of the outline and calculate the two-dimensional Euclidean distance of all points on the image to all points of the outline vectors.

After that the minimum computed distance, d_{min} , of each pixel to all points in the outline was assigned to the image pixel position in a *Distance Matrix*, and the condition tested

$$R_{min} < d_{min}(P) < R_{max} \quad (17)$$

If the condition proves to be true the distance value associated with the pixel were not deleted otherwise it was changed to zero and not consider in the next steps. These has defined a ring shape of points around the crater's center.

The classifier will not receive as inputs an overall crater feature vector but instead will receive an eight feature vector because of the division of the crater in 8 equal slices.

That division was accomplished by measuring the angle that each one of the pixels in the *Distance Matrix* made with the center of the crater previously extracted when the image was translated in polar coordinates for the computation of the edge map

$$\theta(P, C) = \tan^{-1} \left(\frac{y - c_y}{x - c_x} \right). \quad (18)$$

The next step was to assign each to a section label that diferenciate them in each one of the eight sections of the crater. The algorithm scans each section pixel-by-pixel from top to bottom and left to right, and painting with different colors the different labeled pixels within the "crater ring", being easy to visually diferenciate the 8-section ring.

The Figure 2.13 shows the division implemented by this part of the algoritm as well as the location of each section.

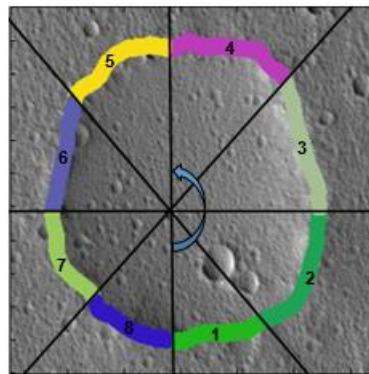


Figure 2.13: Section identification (by numbers and colours)

2.3.1 Gradient Histograms

After the extraction of the gradient features it was necessary to build the corresponding histograms. Thus, it was possible to obtain the distribution of the pixel intensities along the same range of values, is like a form of “quantization”, where we are reducing section gradient vectors to strings of just 8 values and by normalization, despite all gradient vectors having different number of samples, we get equal scaled histograms.

For each section 3 types of gradient were extracted:

- Histogram of Oriented Gradient (HOG), proposed by Dalal and Triggs [21] for human detection task.

Each point of the crater section contributes to the phase histogram with a vote and each vote is proportional to the gradient magnitude so stronger gradients have a bigger impact on the histogram.

The histogram value for the gradient vector of the section s^k is

$$h_i = \sum_{x \in s^k} |g(x)| \times b_i(\varphi(x)) \quad (19)$$

$$b_i(\varphi) = \begin{cases} 1 & \text{if } \varphi \in i^{\text{th}} \text{ bin} \\ 0, & \text{otherwise} \end{cases} \quad (20)$$

the histogram is a horizontal scale of 0 to 2π , so that each bin has a range of 0,785 radians.

- Gradient Phase Histogram proposed by Schiele and Crowley in 2000 [22]
The phase histogram uses the same range system as the weighted histogram, and each point of crater section increases by one the level of the corresponding bin.

The phase histogram value for the gradient vector of section s^k is

$$h_i = \sum_{x \in s^k} b_i(\varphi(x)), \quad (21)$$

$$b_i(\varphi) = \begin{cases} 1 & \text{if } \varphi \in i^{\text{th}} \text{ bin} \\ 0, & \text{otherwise} \end{cases} \quad (22)$$

- Gradient Magnitude Histogram also proposed by Schiele and Crowley in 2000 [22].

The second type of histogram was the magnitude histogram, where each point of the crater section contributes to the magnitude histogram with a vote.

The system of 8 bins stays the same but the maximum value for the range was set based on the maximum value found for the gradient magnitude: 450 units. Therefore we can easily conclude that each bin has a range of 56.25 units.

The magnitude histogram value for the gradient vector of section s^k is

$$h_i = \sum_{x \in s^k} b_i(|g(x)|), \quad (23)$$

$$b_i(|g|) = \begin{cases} 1 & \text{if } |g| \in i^{\text{th}} \text{ bin} \\ 0 & \text{otherwise} \end{cases}. \quad (24)$$

2.3.2 Gradient Percentiles

The second type of feature is the percentiles to the magnitude and direction of the gradient values in each section given the percentage vector. This is a very useful statistic measure to assess the numerical data in a way that lets us know what is the maximum gradient value for each section given the percentile. Percentiles analyzed were the 5th, 25th, 50th, 75th and 95th.

In a ordered data, the K percentile is:

$$P_k = \frac{K(n+1)}{100} \text{ th observation, } n = \text{total observations} \quad (25)$$

2.4. Support Vector Machine Classifier

Support Vector Machines (SVMs) [23] are used to perform image classification, by mapping input feature vectors onto the underlying image class labels. Such a classifier seeks to find the optimal separating hyperplane among different classes by focusing on those training points (named support vectors), which are placed at the edge of the underlying feature vectors and whose removal would change the solution to be found.

The operation of the binary SVM algorithm is based on finding the hyperplane that gives the largest minimum distance to the N training examples: $(x_1, y_1), \dots, (x_N, y_N)$, where $x_i \in R_m$ is a m -dimensional feature vector representing the i^{th} training sample, and $y_i \in \{-1, 1\}$ is the class label of x_i . Therefore, the optimal separating hyperplane maximizes the margin (twice the largest minimum distance) of the training data and is represented with the following expression:

$$w^T x + b = 0, \quad w \in R^m, \quad b \text{ is a scalar} \quad (26)$$

The parameter pair (w, b) corresponding to the optimal hyperplane is the solution to the following optimization problem:

Minimize $L(w)$,

$$L(w) = \frac{1}{2} \|w\|^2 \quad (27)$$

subject to:

$$y_i = (w^T x_i + b) \geq 1, i = 1, \dots, N. \quad (28)$$

When the Training Data is not linearly separable, the SVM uses the concept of soft margin that allows the margin to make a few mistakes (some points as outliers or noisy samples are inside or on the wrong side of the hyperplane). Each misclassified examples contributes to a cost C that is related to the distance to the hyperplane.

The optimization problem solution now becomes:

Minimize $L(w)$,

$$L(w, \xi) = \frac{1}{2} \|w\|^2 + C \sum_{i=1}^N \xi_i \quad (29)$$

subject to:

$$y_i = (w^T x_i + b) \geq 1 - \xi_i, \quad i = 1, \dots, N. \quad (30)$$

$$\xi_i \geq 0, \quad i = 1, \dots, N. \quad (31)$$

When linear SVM does not achieve good results, a nonlinear SVM is used, the basic idea is to map each feature vector x by nonlinearly mapping $\varphi(x)$ to a higher dimensional space in which the optimal hyperplane is found. The Kernel function, $K(x_i, x_j)$ achieves this mapping by computing the inner product of vectors $\varphi(x_i)$ and $\varphi(x_j)$

$$K(x_i, x_j) = \langle \varphi(x_i), \varphi(x_j) \rangle. \quad (42)$$

The most used kernel functions include:

- radial basis function,

$$K(x_i, x_j) = e^{(-\gamma \|x_i - x_j\|^2)}, \quad \gamma > 0. \quad (52)$$

- polynomial function

$$K(x_i, x_j) = (\alpha x_i^T x_j + c)^d. \quad (33)$$

The final stage, the classification stage, uses the following decision function to determine the class label of a sample x which is determined by the sign of the following decision function:

$$f(x) = w^T \varphi(x) + b = \sum_{i=1}^N \alpha_i y_i K(x_i, x) + b. \quad (34)$$

2.4.1 One-against-All Classifier

In this work a Support Vector Machine Algorithm (SVM) of the type One-Versus-All was implemented for the multi-class classification of the data since a ternary label system was previously defined as the best way of aggregate the craters into the categories: well delineated with a well distinguished outline, more and less delineated and bad delineated with a vanished outline.

SVM classifiers were developed for binary classification of data, but as happened in this study this reveals to be quite restricted because craters cannot fit in the model well defined and poorly defined, there must be something intermedium to increase the minuteness of the classification. The ground-truth label defined was ternary, $l \in [1,2,3]$ so the technique used perform pair-wise comparisons between the three classes, creating three binary classifiers that distinguish one class for the other two. The classifier which generates the highest value for its decision function is selected as the winner and the corresponding class label is assigned to the data.

One-against-all approach constructs 3 binary SVM binary classifiers, each of which separates one class from all the rest.

The SVM being test is trained with all the training examples of the i^{th} class with positive labels the other two with negative labels.

When in the training phase, the algorithm uses a function of the LIBSVM library the SVMTRAIN that uses an optimization method to identify support vectors s_i , weights α_i , and bias b that are used to classify the one dimensional feature vectors according to the following equation:

$$c = \sum_{i=1} \alpha_i K(s_i, x) + b, \quad (35)$$

if $c \geq 0$, x is classified as a member of the first group, otherwise it is classified as a member of the second group.

The SVM train algorithm implemented trained a binary classifier for each class $i \in \{0,1,2\}$ as was explain above using for that the LIBSVM function, the SVMTRAIN. The SVMTRAIN trained the three binary classifiers (one against all) to predict the probability of a new instance y belonging to class i . The output of this function was a model of type-struct that retrieves the SVM train parameters:

- nr_class: number of classes;
- totalSV: number of support vectors;
- rho: equivalent to b of the decision function;
- Label: label of each class;
- ProbA: pairwise probability information;
- ProbB: pairwise probability information;
- nSV: number of SVs for each class;
- sv_coef: coefficients for SVs in decision functions;
- SVs: support vectors.

The three retrieved models by the function SVMTRAIN are used in the second stage of the classifier where using as input the matrix of test instance the LIBSVM function SVMPREDICT estimate the probability of each instance of the test matrix belonging to each of the tree model representing the three possible classes to be assigned. The SVMPREDICT will run three times to predict the probability of the test set belonging to each model and returns a probability for each instance belonging to that model or not. A matrix with three columns, representing the probability achieved for each instance to be classified as {0,1,2}, is updated with the probabilities returned by the SVMPREDICT. The final stage is to vote each instance according to the maximum probability obtained for each model in SVMPREDICT and update the Confusion Matrix.

2.4.2 RBF Kernel

The RBF Kernel function was used to train all instances of the training set. This choice was done based on a number of factors. The first one is that this kernel nonlinearly maps samples into a higher dimensional space so, unlike the linear kernel, this function is adapted for the case when the relation between class labels and attributes is nonlinear. Secondly, the number of parameters which influences the complexity of model selection is smaller than in the polynomial kernel. Finally, the RBF kernel has fewer numerical difficulties since $0 < K(x_i, x_j) < 1$, unlike the polynomial kernels, of which the function may go to infinity or zero while the degree changes.

Chapter 3- Experimental Results

3.1. Introduction

Nowadays there are large thousands of images from Mars surface that can be studied by experts, those were mainly acquired since the middle 1970s by NASA and ESA space probes as Viking1, Viking2, Mars Global Surveyor, 2001 Mars Odyssey, Mars Express and Mars Reconnaissance Orbiter, being the last three still in orbit and operating. The evolution on cameras characteristics has allowed a major breakthrough in Image Processing since the resolution of the image just “exploded”. An example of that was the launch in August of 2005 of the HiRISE camera, flying onboard the MRO orbiter. Each image covers an area of 8 to 9.7 kilometers wide with a resolution of 25 cm to 50 cm per pixel. This resolution allows seeing Mars at a level of unprecedented detail because previous images had metric resolution, despite this, HiRISE only represented in 2007, 1% of Mars’s total image surface [24]. These high resolution images from HiRISE were selected for the development and testing of the methodology in this thesis due to the higher details that can be perceived.

In this chapter it is described the experimental procedures, namely the construction of the datasets, the division of the images into the Training and Test Sets, the selection of the parameters of the classifiers as well as the evaluation statistics used to quantify the results of the classifiers. The results obtained for the different features are then analyzed and discussed.

3.2. Image Datasets

Two distinct regions or sets from Mars were selected to develop and test the methodology (Figure 3.1): Set 1 consists of a younger surface region of plain characteristics (image with a smooth texture) located in the northern hemisphere (29,57°N-371,51°E), while Set 2 consists of an much more irregular surface (image with a varied texture) located in the southern one (13.94°S-69.60°E). Each set is covered by one single HiRISE image (ESP_011491_2090 for Set 1 and ESP_025555_1940 for

Set 2). The two different resolutions provided by HiRISE images were also taken into account (0.25 cm/pixel for image in Set 1, and 0.50 cm/pixel for image of Set 2) to better evaluate the approach.

Both Data Sets images have been taken in 2009. It is easy just by visual analysis to differentiate some craters in terms of shape, size and delineation.

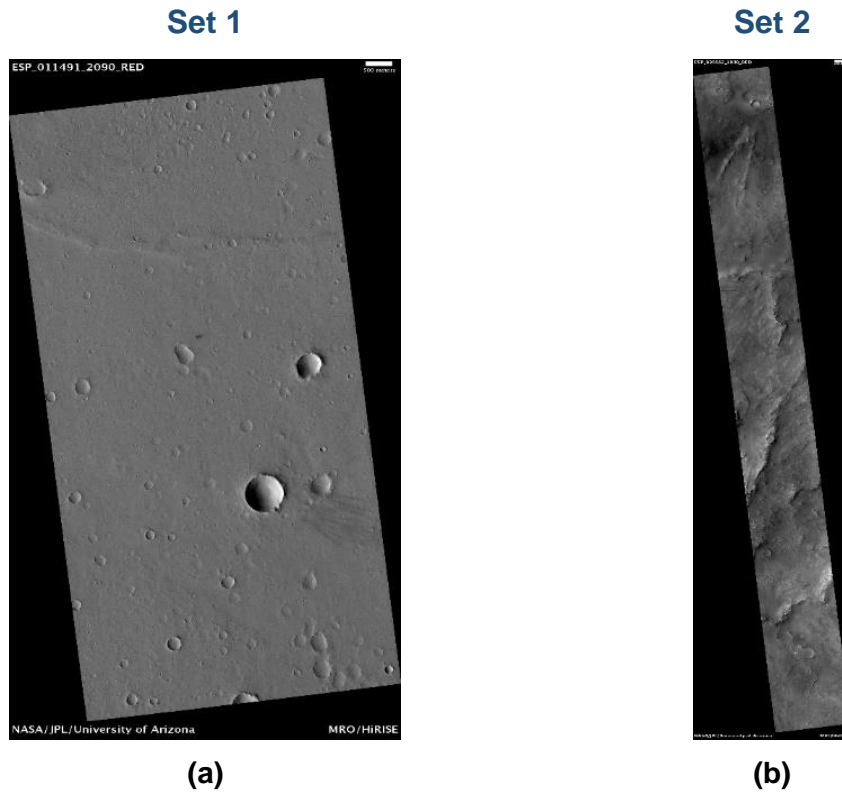


Figure 3.1: Overview of the two analyzed regions: (a) Recent Impacts- Lunae Palus quadrangle, Scale:25 cm/pixel; (b) Layered Ejecta near Syrtis Major quadrangle, Scale :50cm /pixel

In Table 3.1 are shown the details for each selected site, namely the location on Mars according to longitude and latitude in decimal degrees, the image resolution as well as the total number of craters selected in each site.

Site #	Camera	Image <i>id</i>	Lat °	Long °	Resolution <i>m/pixel</i>	Craters <i>Nb</i>	Diameter(m)		
							<i>min</i>	<i>max</i>	<i>avg</i>
1	HiRISE	ESP_011491_2090	29,57N	371,51E	0.25	60	9	722	67
2	HiRISE	ESP_025555_1940	13.94S	69.60E	0.50	110	10	585	165

Table 3.1: HiRISE images and craters Datasets

The algorithm was tested over two DataSets of crater images sampled from the two region images in Figure 3.1. The first one (named DataSet1) is constituted by a total of 60 crater images (480 sections). In Figure 3.2 it is possible to see four samples of different dimensions craters and distinguish the 3 degrees of preservation. The P037 crater is the one that comes closer to a preserved crater (type 0), with some portions of well-defined rim. The craters P005 and P032 are modified craters (Type 1) with significant signs of erosion reflected in the state of the rim. The P046 is a highly degraded crater (type 2) where the rim is no longer distinguishable in certain and large regions of the contour, however it is still possible to distinguish the crater rim in some areas and that those fit the type 2 crater category.

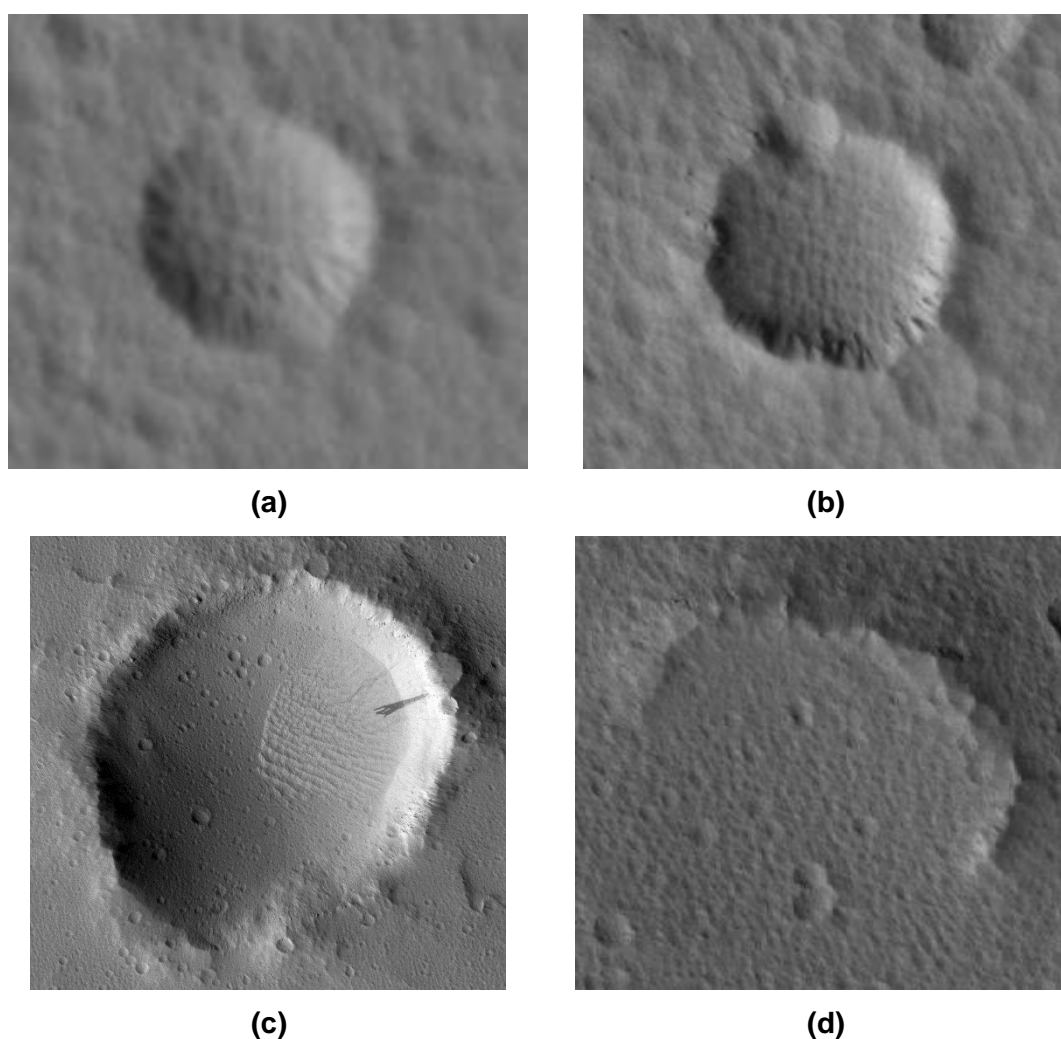


Figure 3.2 : Sample Images of DataSet1 with different sizes and preservation degree: (a) Crater p005-Image dimension: 146×127 pixels, crater radius:36 pixels; (b) Crater p032-Image dimension: 268×252pixels,crater radius:69 pixels;(c) Crater p037-Image dimension:2452×2345pixels, crater radius:963 pixels;(d) Crater p046-Image dimension: 703×675 pixels, crater radius:256 pixels

The second DataSet, named DataSet2, consists of 110 images (880 sections). In Figure 3.3 we can see some samples of images in this set. The p034 crater is a globally well-preserved crater (type 0) due to its rounded shape and its well evidenced rim. The crater p055 is a crater of type 1 (modified) by its irregular rim and flat appearance, however are visible areas of type 3. The p022 is a degraded crater (type 2) but with some rim zones characterized as type 1. Finally in the image p087 it is possible to identify an overlap situation between two craters. Two contours were possible to be detected. The outline of the crater detected by the DP algorithm was the one from the crater located more above. In this case the algorithm will outline zones belonging to the lower crater which leads to results that do not correspond to the reality.

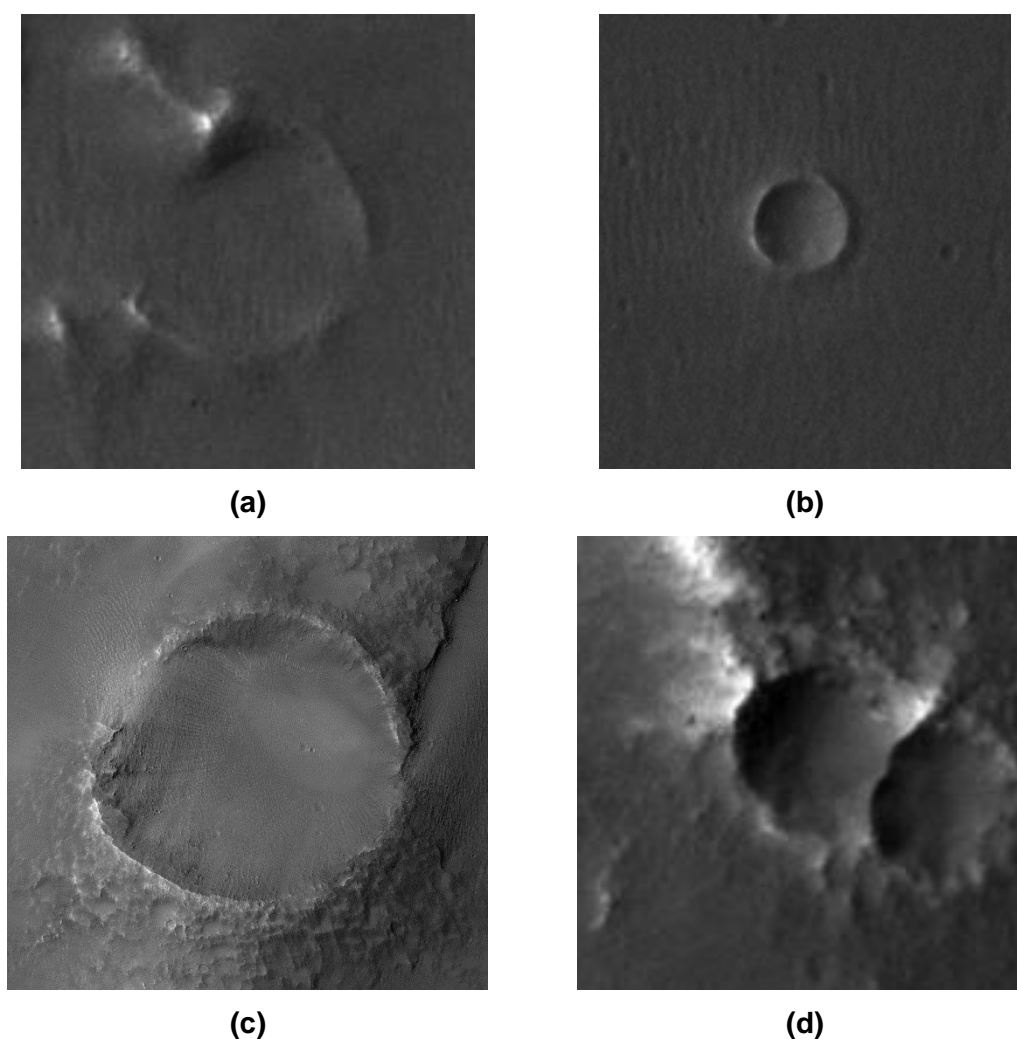


Figure 3.3: Sample Images of DataSet2 with different sizes, preservation degree and overlap situation in image p087: (a) Crater p022-Image dimension: 191×191 pixels, crater radius:50 pixels; (b) Crater p034-Image dimension: 176×194pixels,crater radius:21pixels;(c) Crater p037-Image dimension:1673×1769pixels, crater radius:569 pixels;(d) Crater p087-Image dimension: 155×155 pixels, crater radius:34 pixels

The HiRISE images correspond to the red band of the electromagnetic spectrum, are in grey scale (8 bits or 256 levels) and the dimensions vary for image to image, according to the dimension of the crater. The scale of the DataSet 1 images has twice the resolution of the one of DataSet 2, as we can see on Table 3.1. For DataSet 1 the largest crater image has the dimension of 3561x3485 pixels, while the smallest measures 62x61 pixels with an average of 386x404 pixels. For DataSet 2 the largest image has the dimension of 1673x1769 pixels, while the smallest measure 26x27 pixels, with an average of 235x249 pixels. This DataSet contains 26 images with a size inferior to the size of the smallest crater in DataSet 1.

3.3. Ground-truth construction

For the construction of the classifier, as well as for the evaluation of its performance, it is necessary to label each crater section with its degradation state.

Three labels were considered in this study: '0' for preserved or sharp rims along the whole sector, '2' for strongly degraded and/or missing rims and '1' for situations falling within the two previous extreme situations. These labels were assigned to each section of every crater of the datasets by an expert through qualitative visual inspection. Some examples of this labelling are shown in Figure 3.4. This information, to be used in a crucial phase of this project, is generically called the ground truth (GT) or reference data, and is used in the training phase of the classifier and also in the validation of its performance/accuracy in the test phase. The GT is a 480 position label vector.

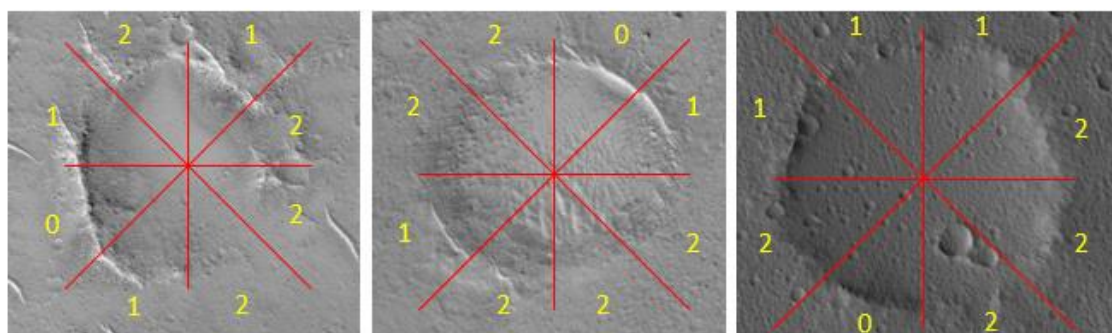


Figure 3.4: Part of the GT for the Data

3.4. Evaluation Criteria

3.4.1 Cross Validation

To enlarge the viability of the classifier and to avoid the overfitting situation, caused by a repetition of the same data in the prediction phase and in the training phase, leading in this way to a deceiving “perfect” score, the strategy was to use a rotation model called Cross-Validation.

It was necessary to define which images were part of the learning phase and which ones are going to test the performance of the classifier. Since the two Dataset dimensions are not large, the decision was to use 59/109 craters (Dataset1/Dataset2) to train the classifier and only one crater to test it, using the Cross Validation strategy repeating this way the process 60/110 times. The overall performance consists of the average of all individual performances.

Since the features that are being used are related to each section of each individual crater and not to the whole crater itself, the quantities at each step of the cross-validation procedure consist of 472/872 vectors for training the classifier and the remaining 8 to test it. This way, each group of eight sections (one crater) is used once for validation and 59 times for training.

3.4.2 SVMTRAIN parameters

The SVM kernel (RBF) uses 2 parameters to train each training set. Choosing the best combination of both that leads to the best accuracy in each iteration of the Cross Validation was one of the steps to properly train the classifier. This parameter selection was achieved using Nested Cross Validation, represented in Figure 3.5, where the inner loop is used to perform the tuning of the parameters while the outer loop of the Cross Validation is used to compute an estimate of the model error.

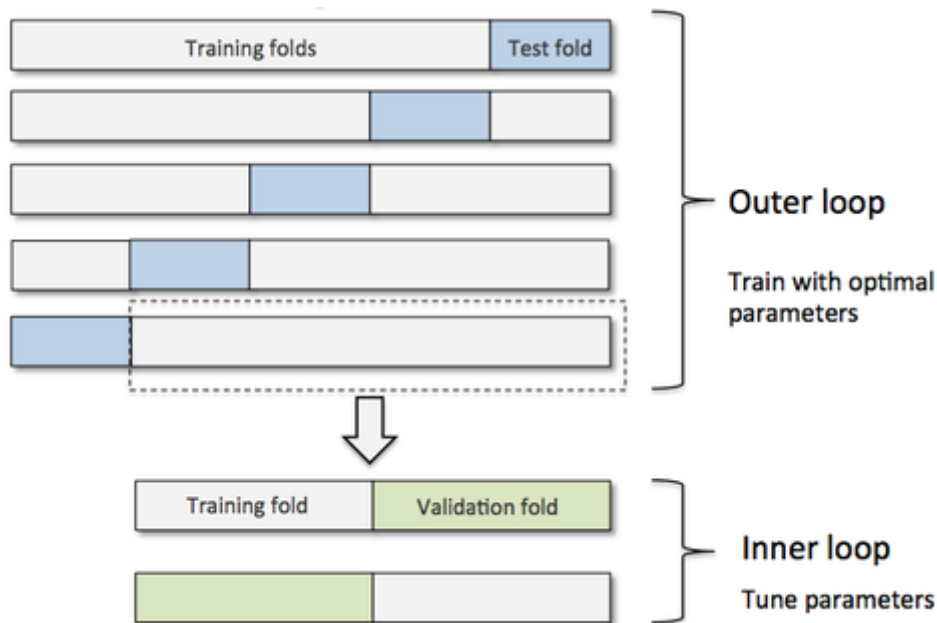


Figure 2.5: Nested Cross Validation for parameters optimization

The penalty parameter C balances the misclassification of the training examples against the simplicity of the surface. A lower value of C leads to a smoother decision surface while the opposite aims to a correctly classification of all training instances.

The behavior of the model is also affected by the other parameter, the gamma parameter. If gamma is too large, the radius of the area of influence of the support vectors only includes the support vector it-self and no amount of regularization with C will be able to prevent overfitting. When is very small, the model is too constrained and does not adjust itself to the shape of the data.

The strategy implemented was to make the parameters sequence to grow exponentially and duplicate its value for each cycle of the parameter selection. The inner cycle used for parameter selection uses 2 cycles, the outer cycle responsible for varying the C values and the inner cycle responsible for the variation of the gamma value.

The initial and final values of C and gamma were 2^{-6} and 2^6 and for each iteration of the training set the inner cycle (C parameter) and outer cycle (gamma parameter) of the parameters was ran and the best pair, the one that reaches the highest accuracy, was chosen and used to train the training set.

Each C and gamma pair of values was saved for each training and test iteration. The accuracy achieved for those parameters and the pair and the accuracy that leads to a maximum value of accuracy was saved for estimation of the final accuracy value. Finally the classifier used that same parameter values to train the classifier.

3.4.3 Final Statistics: Confusion Matrix and Final Accuracy

To evaluate the performance of the entire algorithm, the Confusion Matrix was built to calculate the overall accuracy.

The Confusion Matrix is a Table that allows to count the correct and the wrong classifications returned by the classifier. Each column of the matrix represents the instances in a predicted class while each row represents the instances in the actual class. In each one of the 60/110 cycles of the algorithm, the confusion matrix was updated 8 times for the 8 section.

A performance of 100% would fill only the principal diagonal of the confusion matrix.

The confusion matrix is updated at each iteration by adding one more unit to the value previously recorded for that cell. The formula used to update the matrix was the following, the i is the instance being updated (1 to 8), and the Score is the classification predicted by the classifier:

$$\text{Confusion_matrix}(\text{GT}(i), \text{Score}(i)) = \text{Confusion_matrix}(\text{GT}(i), \text{Score}(i)) + 1 \quad (36)$$

Finally, the Overall Accuracy of the classifier which used the Accuracy Matrix to measure the percentage of correct classifications was calculated,

$$\text{Final Accuracy} = \frac{\sum_{i=1}^{nc} e_{ii}}{\text{Number of instances}}, \quad e_{ii} = \text{position of the matrix cell} \quad (37)$$

where the number of instances are:

$$N = \sum_{i=1}^{nc} \sum_{j=1}^{nr} e_{ij}, \quad nc = \text{number of columns}, \quad nr = \text{number of rows}. \quad (38)$$

3.5. Classifier Results

3.5.1 DataSet1 results

3.5.1.1 Histogram gradient features results

The SVM classifier was tested separately using 3 types of features:

- Type 1: Gradient Magnitude Histograms,
- Type 2: Gradient Phase Histograms and
- Type 3: HOG features.

Table 3.2 shows the results for the three classifiers using the histograms as features, revealing that using phase histograms leads to insignificant improvements in final accuracy. All achieved classification results in the order of 80%. The classifier that had the best performance was the one using type 1 features, achieving a classification accuracy of 81,6%.

SVM classifiers statistics using histograms as feature vectors-Data Set1														
Features type 1 : Gradient Magnitude Histograms				Features type 2 : Gradient Phase Histograms				Features type 3: HOG						
Predicted class				Predicted class				Predicted class						
Actual class		0	1	2	Actual class		0	1	2	Actual class		0	1	2
	0	7	22	0		0	1	28	0		0	0	29	0
	1	0	311	6		1	0	311	6		1	0	311	6
	2	0	60	74		2	0	55	79		2	0	60	74
Final Accuracy≈ 81,6%				Final Accuracy≈ 81,5%				Final Accuracy≈ 80,0%						

Table 3.2 Statistic Results for Data Set1 using histogram as feature vectors

The first classifier using the histogram gradient's magnitude of each section has achieved 392 correct identifications out of 480 samples, the second classifier using the histogram gradient's phase achieved 391 well classified sections and the last the weighted histogram with 385 properly classified sections.

From the 29 well delineated/relatively recent sections (labelled as 0) the first classifier was the one that performed better, putting 7 with the correct label and 22 with label 1 (intermedium state of conservation). The second classifier identified correctly only 1 sections and the others 28 labeled as section '1'. The weighted histogram was not able to identify any. Obviously the 3 classifiers were having troubles distinguishing the "0" section from the '1' section.

When the data belongs to the "intermedium" class the results are much more satisfying since only 6 of a total of 317 sections are being incorrectly assigned to his true group by the three SVM classifiers. Being the majority class (66% of the total Data), the classifier is obviously more prepared to distinguish it from the others because the classifier could learn a major number of patterns for this type of feature. This leads us to one of the answers for not having even better results on the accuracy, since SVM classifiers trained on an unbalanced dataset often produce models which are biased towards the majority class and have low performance on the minority class as presented in this case. It has been identified that the separating hyperplane of an unbalanced SVM model can be skewed towards the minority class [25] and this skewness can degrade the performance of that model with respect to the minority class.

When the class is the one that is bad delineated, which represents 134 of the 480 sections, we can see that it is the second class with more data and the accuracy values achieved were approximately: 55%, 59% and 55% for each of the three classifiers (in that order) .

To properly understand why the performance is not achieving adequate results for some specific cases, it can be more enlightening to review the feature histograms and the algorithm classification results for the phase and magnitude histogram classifiers. These are the classifiers that stand out by surpassing the main difficulties of the algorithm: distinguish the 0 label of the 1 label and the 2 label of the 1 label. The SVM classifier that used weighted histograms has not reached satisfying results.

Features type1, classifier results:

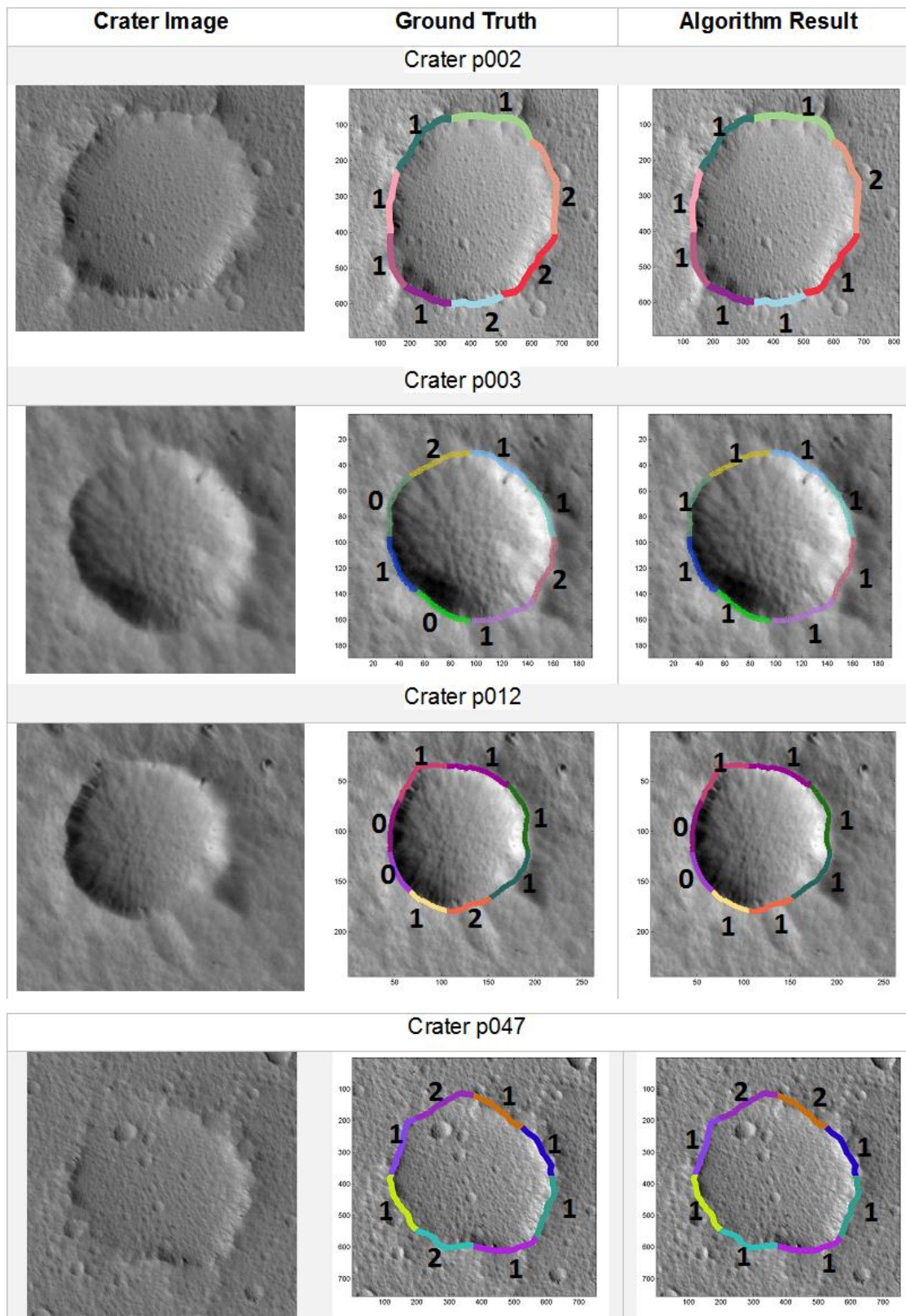


Figure 3.6: Performance examples for SVM classification with features type 1: (left) input image, (center) GT and (right) Algorithm result. ('0' means preserved, '1' moderately preserved/degraded and '2' degraded)

By analyzing the examples shown in Figure 3.6 we get a better acquaintance of the results achieved by the developed algorithm (right) in comparison with the real image (left) and with the GT image (center). These examples show rapidly the situations where the classifier behavior is reliable and those where it has not achieved the correct classification.

As is clear in Figure 3.6, the outline of p002 crater is not uniform, with sections where the rim is more accentuated than in others. The computational results obtained in the extraction of the histograms are this in some situations ambiguous and may explain why the algorithm was not able to proper classify two of the eight regions. In Figure 3.7 it is presented the normalized histogram feature vectors for each section.

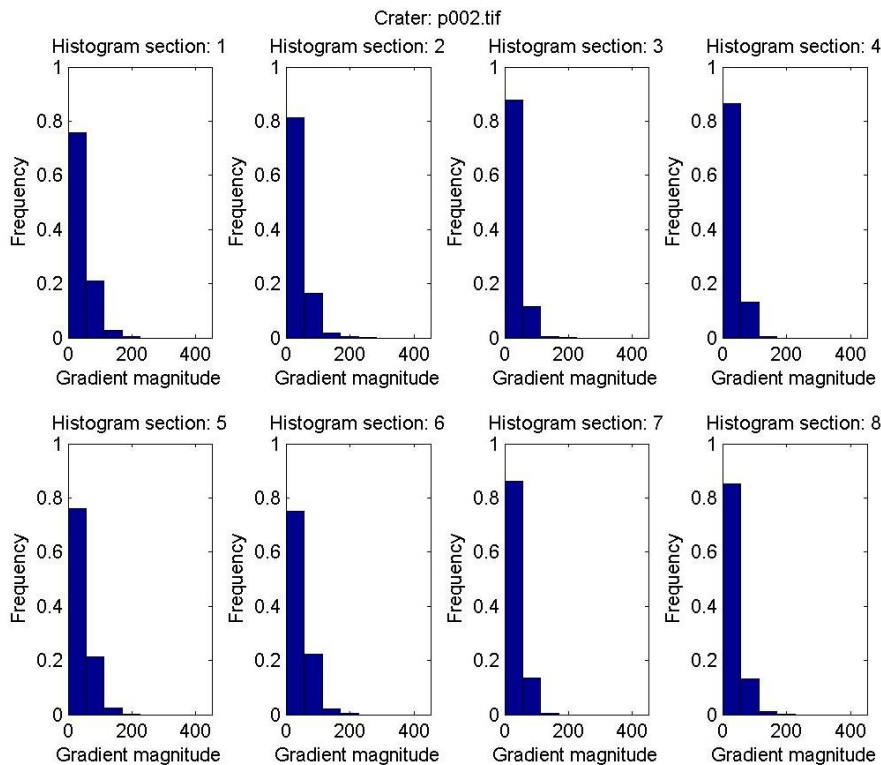


Figure 3.7: Crater p002 gradient magnitude histograms

All the 8 histograms have a similar behavior, the first bin which represents the lowest interval of gradient values, is largely the most frequented (approximately 80% in each of the 8 sections) while the highest magnitudes do not have any samples. This is obviously an example of a not well-defined or well-preserved crater.

Only section 3 was classified as '2' and looking to the histograms we can see that it is the one that as about 90% of extracted points in bin number 1 (with a range of 0-56,25 units), and the rest of the percentage falls in the second bin (with a range of 56.25-112,5 units), having approximately 1% into 3rd bin . Histograms of section 1 and

2 (with a GT of 2) are much alike the histograms of section 5 and 6 (with a GT of '1'), so it is understandable that the classifier had difficulties in distinguishing them and has classified it as a section of type '1'.

Craters p003 and craters p012 are two examples where the algorithm did not reach a not so reliable classification. In crater p003 the algorithm was not able to distinguish the two '0' sections, sections 6 and 8, signed into GT. For crater p012 the same happened to sections 6 and 7. To a further comprehension, the figures below show the differences in the histograms.

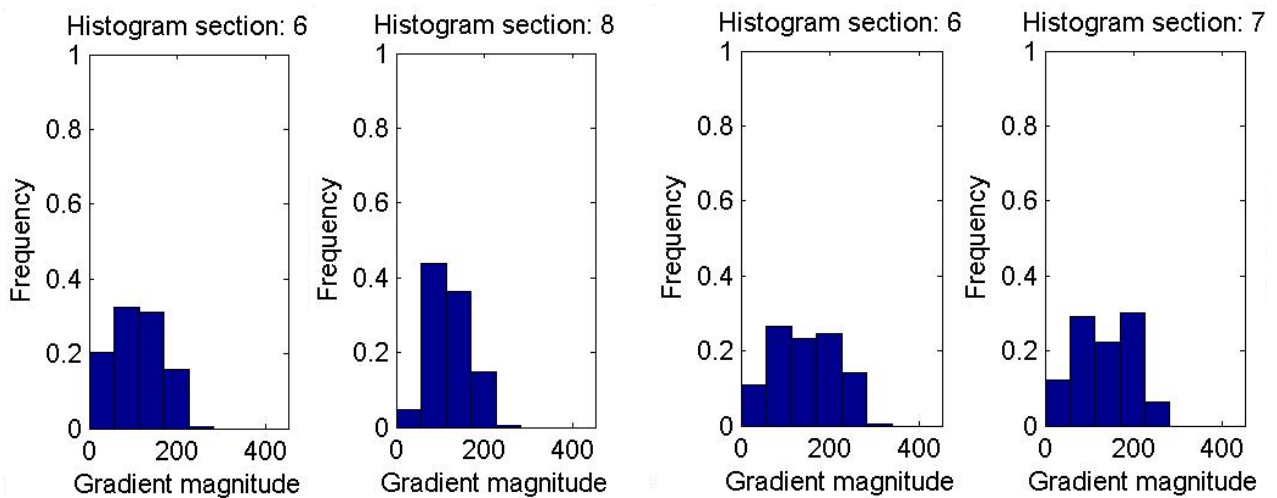


Figure 3.8: Crater p003 sections with GT '0'

Figure 3.9: Crater p012 sections with GT '0'

The Figure 3.8 shows the crater p003 histograms of sections 6 and 8, that the algorithm does not classify as '0'. Figure 3.9 shows the crater p012 histograms for the sections 6 and 7 that were correctly assigned by the algorithm into '0' category. It is possible to conclude, that the histograms on the right have a highest percentage of points into bin 5 (281,25-337,5 units) which represent the highest gradient magnitude values. The histograms on the left has more samples in the lower gradient bins and the fifth bin has almost zero samples in its range. This difference in the distribution can possibly explain the 2 mis-classification cases in crater p003.

In the misclassification in crater p047 the algorithm follows the same pattern as the one discussed for the crater p002. There is a correct assignment of section 3 to label '2' and a misclassification of section 4 into label 2 instead of label 1 and of section 8 into label 1 instead of label 2. Figure 3.10 shows that the pattern of having 90% or more of the points in the first bin and almost the rest in the second was learned by the classifier as a behavior of features related to the section of badly defined crater section. The misclassification of 60 sections into label 1 instead of 2 as well as the 6

misclassifications of label 1 into label 2 occurs mainly because of the distribution of points into the first 3 histogram bins. Small differences can be enough to the classifier label the sections into the wrong category.

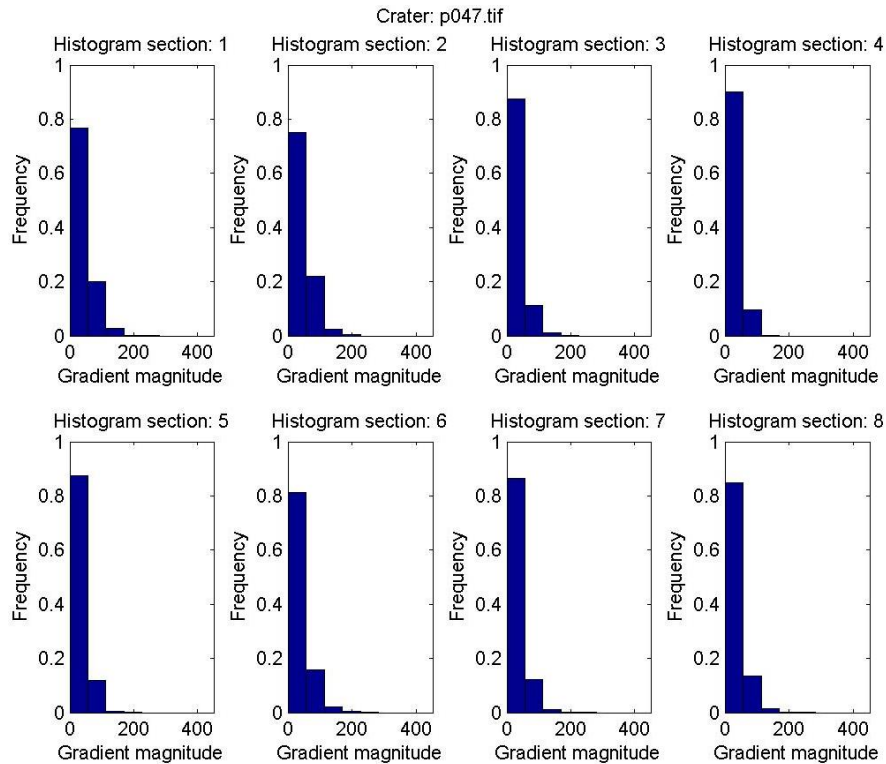


Figure 3.10: Crater p047 gradient magnitude histograms

Features type2, classifier results:

This classifier stands out by being able to classify correctly the sections of type 2 and not confusing them with sections of type 1. The major weakness relies on the correct classification of only 1 of the 29 sections of type 1.

The 8 bins of the histogram are the different directions from 0 to 2π , and the value of each bin corresponds to the number of section points with intensity changes noted in that direction. The histogram peaks correspond to the dominant orientations. Notice that the gradient vectors do not point along the edge, but normal to it.

It is expected that a region with a relative sharp edge reflects into a histogram with a strong peak with a normal direction to the edge. A well-defined curve edge would reflect into a histogram pointing directions depending on exactly where along the edge the points were taken. Finally a section with no texture, with few interest points would

have gradients with random directions possibly reflecting a low energy and uniform histogram.

To a better comprehension of the strengths and weaknesses of this classifier let us visually compare some of the results obtained (see Figure 3.8).

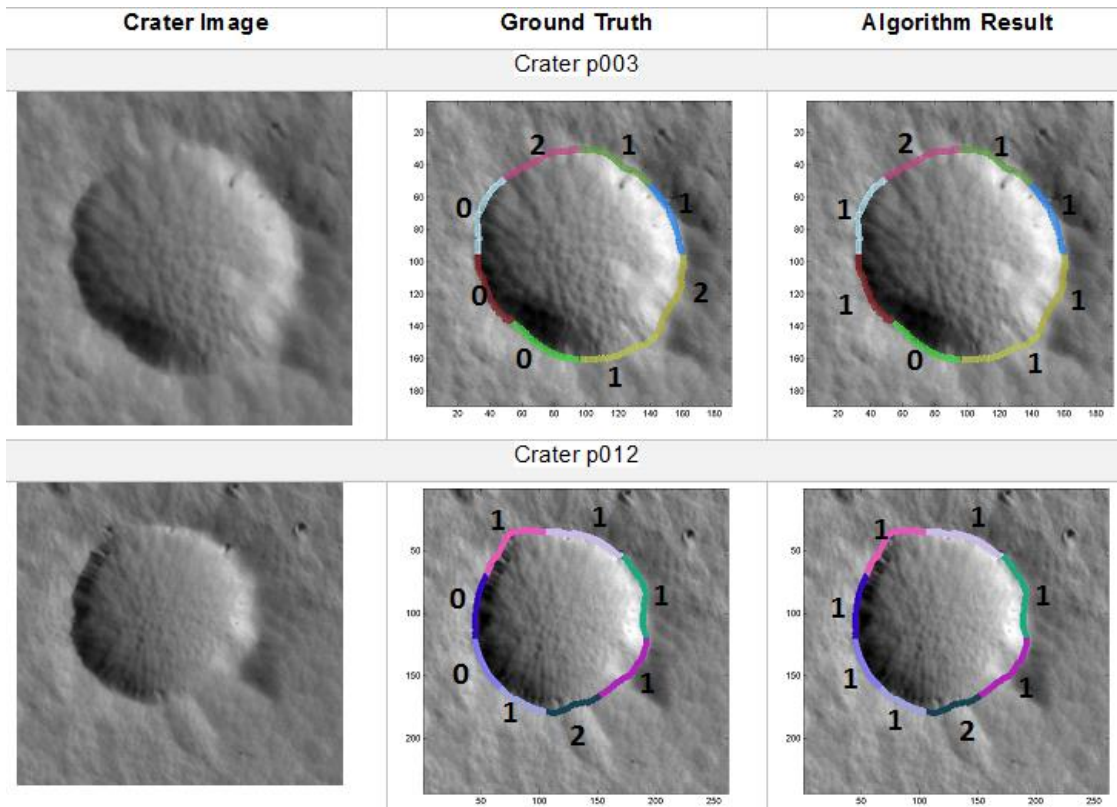


Figure 3.11: Performance examples for SVM classification with features type 2: (left) input image, (center) GT and (right) Algorithm result. ('0' means preserved, '1' moderately preserved/degraded and '2' degraded)

These two examples on Figure 3.8 are ideal to illustrate that a constant pattern does not exist mainly for the sections of type '1'. Craters of type '0' have in many sections a histogram with similar characteristics to some of craters histograms of type '1'. This can explain the 28 mis-classifications of this type achieved by the classifier. It is possible to see (Figure 3.9) that sections 6 and 7, that have a GT of '0' and also have 3 major peaks, well differentiated between the three, the one in the middle with more impact than the other two. This is the pattern that the classifier associates to this kind of section. This represents the direction of the points in the section.

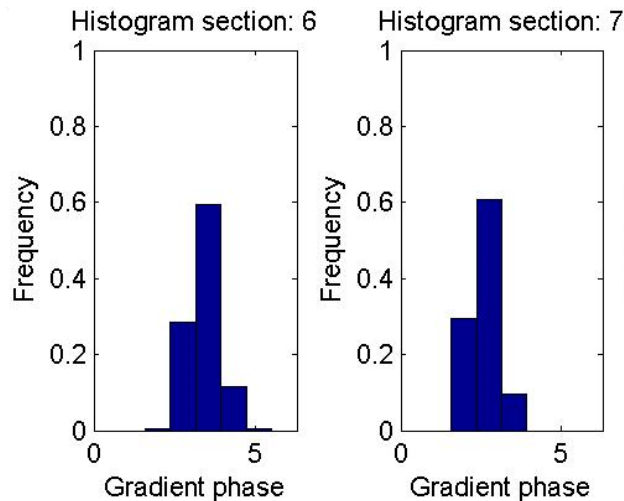


Figure 3.9: The two sections of crater p012 with GT = '0'

Analyzing the histograms of crater p003 (Figure 3.10), both sections 6 and 8 have GT equal to '0' but only the 8th was classified as 0'. Yet, it is possible to see in crater p003 that sections 2, 4 and 7 a have a similar behavior to the one in section 6 and have a GT classification of '1'. This situation happens often, so while training the classifier it has learned with greater frequency that this is a characteristic behavior for the histogram sections of type 1 and because of that it associates them to this category.

In the other hand crater section of type 2 does not offer so many doubts to the classifier that relates this category to histograms with samples relatively uniform distributed for all the bins as happened in the section 5 of crater p003. A normal behavior of this kind of histogram is that the higher impact bin does not surpasses 0.2 in the frequency value. The mis-classification of type '2' in type '1' in crater p002, is understandable, the appearance of the rim is visually similar to the section rims around it classified as '1'. It is observed that the similarity between the histograms in Figure 3.9 replicates the topic discussed above where craters of type '0' can be confused with craters of type '1'. The section histogram reflects this idea.

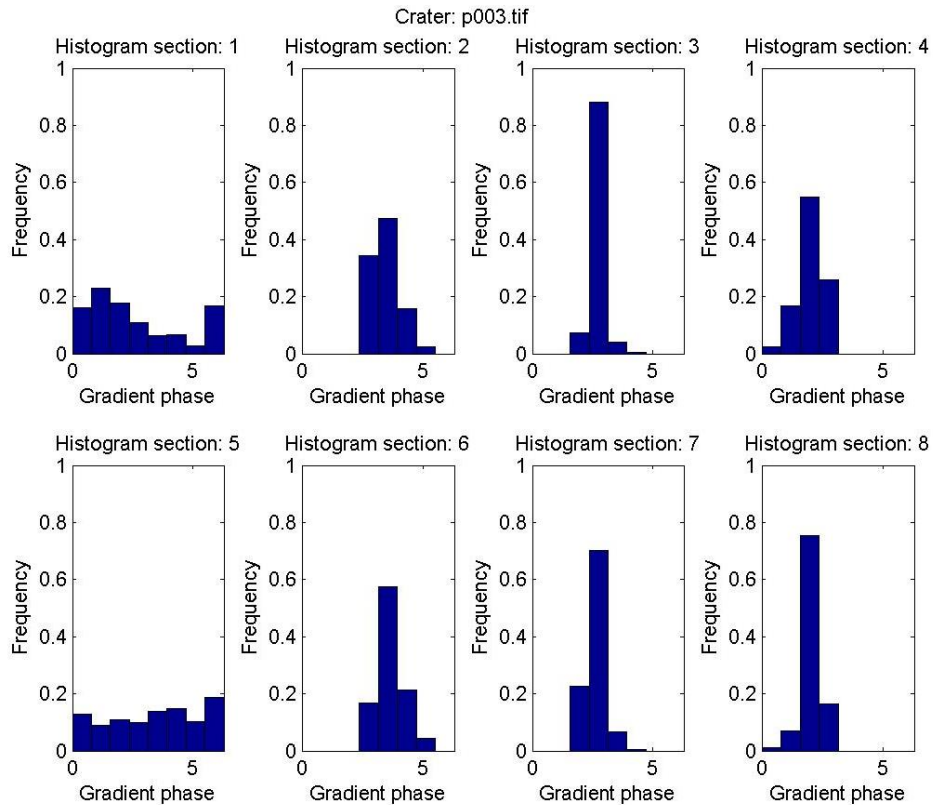


Figure 3.10 Crater p003 gradient phase histograms

3.5.1.2 Percentile features results

The percentiles features were calculated in each crater section using the gradient magnitude and direction value extracted for each pixel. The percentiles calculated over each section were the 5th, 25th, 50th, 75th and 95th, then all were aggregated in a single vector and used as feature vectors. This kind of feature despite being very simple and computationally light-weight has shown to perform well in visual inspection problems[26]. The k percentile gave us the maximum gradient value that fall below each percentage, and could give a good perspective of the distribution of data. The results obtained with this kind of features are shown in Table 3.3.

The SVM classifier was also tested separately using another 2 type of features:

- Type 4: Percentiles vectors of the magnitude gradient sections and
- Type 5: Percentiles vectors of the direction gradient sections.

Table 3.3 shows the results for the three classifiers using the gradient percentiles as features, revealing that using phase histograms as happened for histograms, leads to improvements, this time ~5% in final accuracy

The results however proved that their simple complexity were not enough to overcome with efficiency problems such as the closest appearance of type '1' and type '2' rim and the results fell short in distinguishing the type '2' from type '1'. However it is relevant to point that while distinguishing those two states of preservation, the gradient phase histograms prevailed over the classification results of the gradient magnitude histograms and also the percentiles of the gradient phase performed better than the percentiles of the gradient magnitude. This consistency ends up making sense.

The correct classification of type '0' sections failed by the proximity in gradient values with sections of type '1'.

Once more the major difficulty arises in the variety of patterns that type '1' crater exhibit. For instance, some of the modified examples still have a significant amount of pixels with relevant intensity variations. But other examples are modified in a way that the percentage of points of interest exceeds for very little the percentage in type '2' craters.

SVM classifiers statistics using gradient percentiles as feature vectors- DataSet1				
Features type 4: Percentiles vectors of the magnitude gradient sections			Features type 5: Percentiles vectors of the phase gradient section	
Actual class	Predicted class			
		0	1	2
	0	0	29	0
	1	0	315	2
	2	0	111	23
Final Accuracy ≈ 70%				
Actual class	Predicted class			
		0	1	2
	0	0	29	0
	1	0	316	1
	2	0	88	46
Final Accuracy ≈ 75,4%				

Table 3.3: Statistic Results for Data Set1 using data percentiles as feature vectors

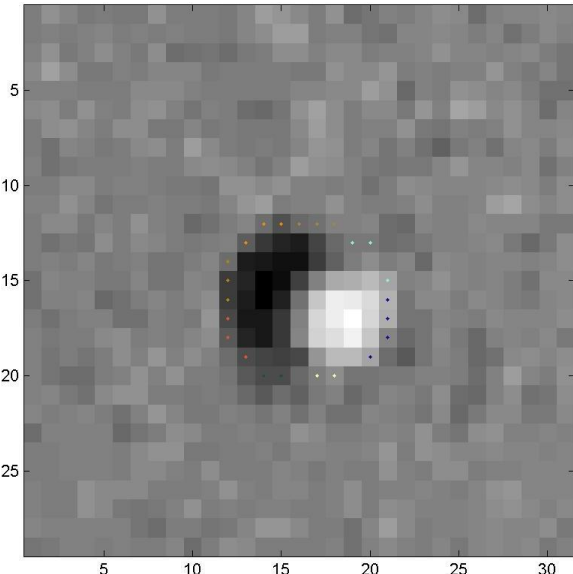
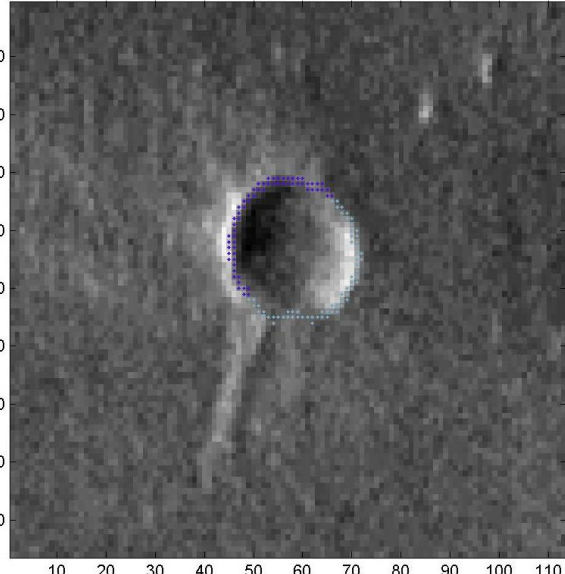
3.5.2 DataSet2 results

The procedure for the classification of the sectors of the samples constituting DataSet2 are shown in Table 3.4. Globally, it can be concluded that for this Data Set the results were considerably less satisfying.

Since the algorithm was dealing with images much smaller and with considerable less definition than those in DataSet1 the histogram features were compromised.

In some situations the image has reasonable dimensions but the crater on it does not (crater p044 is an example of that). Because of that only two or three sections could be extracted in this example and the other 6 or 7 histograms were completely nulls as exemplified in crater p044.

In other situations the dimension of the images is too small but the crater image itself occupied almost the entire image, so the algorithm could hardly distinguish the 8 sections in a correct way. In this case, the points do not represent well the sections (the amount of extracted points in this case are less than a dozen) and the lack of definition of the image prevents the possibility of distinguishing the contour like in the crater p015.

<p align="center">Crater p015</p> <p align="center">Image Dimension:31x29 pixels</p> <p align="center">Crater Radius:5 pixels</p>	<p align="center">Crater p044</p> <p align="center">Image Dimension:113x96 pixels</p> <p align="center">Crater Radius:13 pixels</p>
	
<p align="center">Crater p015 gradient magnitude histograms</p>	<p align="center">Crater p044 gradient magnitude histograms</p>

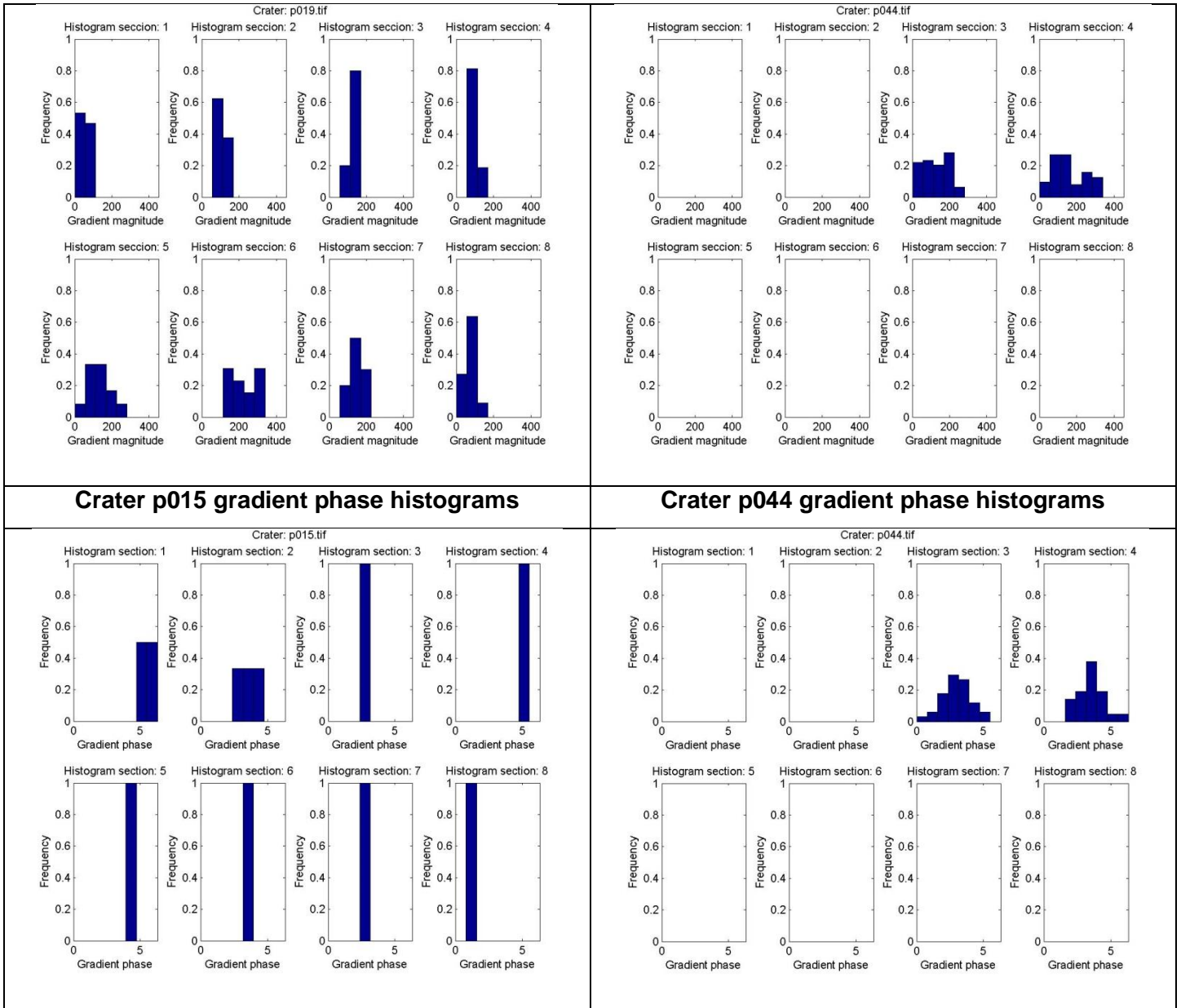


Table 3.4: Two examples were the algorithm fails due to craters small size

These two situations are verified in a total of 51 images (408 sections) of DataSet2 damaging the training phase of the classifier that learnt wrong behaviors for the section histograms. This was the main reason for the poor results achieved by the three types of histogram section classifiers. The results were ~26% for the three classifiers that were not able to define a learning pattern for each section category classifying all the craters as belonging to type '2' (Table 3.5)

SVM classifiers statistics using histograms as feature vectors-DataSet2														
Features type 1 : Gradient Magnitude Histograms				Features type 2 : Gradient Phase Histograms				Features type 3: HOG						
Predicted class				Predicted class				Predicted class						
Actual class		0	1	2	Actual class		0	1	2	Actual class		0	1	2
	0	0	0	106		0	0	0	106		0	0	0	106
	1	0	0	542		1	0	0	542		1	0	0	542
	2	0	0	232		2	0	0	232		2	0	0	232
Final Accuracy≈26 %				Final Accuracy≈ 26%				Final Accuracy≈ 26%						

Table 3.5 Statistic Results for the entire Data Set2 using histogram as feature vectors

Also the percentiles were compromised with a classification around 26%(Table 3.6) because of the two problems pointed before, the classification results are equal to the other 3 feature types revealing once more that the learning phase was completely compromised.

SVM classifiers statistics using gradient percentiles as feature vectors-DataSet1														
Features type 4: Percentiles vectors of the magnitude gradient sections						Features type 5: Percentiles vectors of the phase gradient section								
Predicted class						Predicted class								
Actual class		0	1	2	Actual class		0	1	2	Actual class		0	1	2
	0	0	0	106		0	0	0	106		0	0	0	106
	1	0	0	542		1	0	0	542		1	0	0	542
	2	0	0	232		2	0	0	232		2	0	0	232
Final Accuracy≈ 26%						Final Accuracy≈ 26%								

Table 3.6: Statistic Results for the entire Data Set2 using data percentiles as feature vectors

It is safe to affirm that the algorithm is not able to perform well when the crater radius is less than 16 pixels.

The strategy was to remove those craters and run the algorithm so that the classifier could be trained properly.

The overall results for the histogram features were approximately 70% as it's possible to see in Table 3.7. The results fell in about 10% when compared with the results of DataSet1.

SVM classifiers statistics using histograms as feature vectors-DataSet2																	
Features type 1 : Gradient Magnitude Histograms				Features type 2 : Gradient Phase Histograms				Features type 3: HOG									
Predicted class				Predicted class				Predicted class									
Actual class				0			1			2			Actual class				
				0	15	42	0	0	2	55	0	0			0	57	0
				1	0	279	29	1	0	278	30	1			0	280	28
				2	0	67	40	2	0	49	58	2			0	51	56
Final Accuracy ≈ 70%				Final Accuracy ≈ 71%				Final Accuracy ≈ 71%									

Table 3.7 Statistic Results for part of Data Set2 using histogram as feature vectors

This situation could be explained by the fact that this DataSet has samples with a larger ambiguity. For some sections and also for entire craters it becomes harder to assign them into an obvious GT. Ambiguous GT lead to ambiguous results. The increase of the error in GT is the explanation for the decrease in the results. Also the presence of situations of superposition (Figure 3.11) between two craters that does not existed in the DataSet1 led the Dynamic Programming Algorithm to detect a wrong part of the crater outline which had impact in the extracted features.

In this particular situation the well delineated contour of the crater, classified as type '1' in GT was classified as '2' by the algorithm because of the homogeneous region from where the features were extracted.

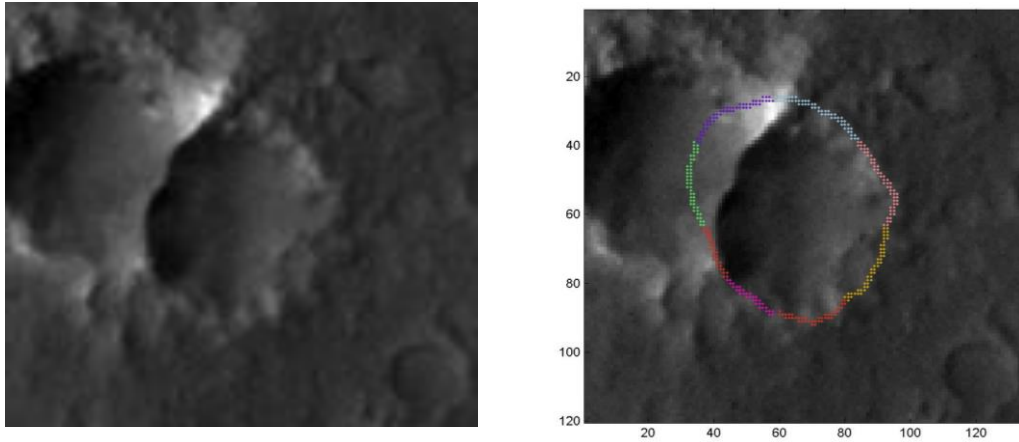


Figure 3.11: Feature extraction in case of superposition between two craters

The accuracy of this DataSet decreases mainly due to the algorithm's failure to classify type '0' craters while using features of type 1.

When using features of type 2, the accuracy decreases because the algorithm has more difficulty on distinguishing the craters of type '2', categorizing them with more frequency into type '1' craters, than in the DataSet1. The dimension of the craters had also influence in the decrease of the results. Those were quite similar in DataSet1 and for DataSet2 had oscillations, with craters with dimensions considerable bigger than others. This also led to an oscillation in the pattern of learning for each type of preservation state.

The pattern for the type 1 and type 2 features follows, with less accuracy, the rules for DataSet1 and for that reason were not illustrated.

The percentiles of gradient magnitude and phase had an accuracy of approximately 60% revealing to be in concordance with the histogram results as DataSet1 (Table 3.7).

SVM classifiers statistics using gradient percentiles as feature vectors- DataSet2									
Features type 4: Percentiles vectors of the magnitude gradient sections			Features type 5: Percentiles vectors of the phase gradient section						
Predicted class			Predicted class						
Actual class		0	1	2	Actual class		0	1	2
	0	0	57	0		0	0	57	0
	1	0	273	20		1	0	270	23
	2	0	83	26		2	0	75	32
Final Accuracy≈ 63%			Final Accuracy≈ 64%						

Table 3.8: Statistic Results for part of Data Set2 using data percentiles as feature vectors

Chapter 4- Conclusions and Future work

The purpose of the methodology implemented in this project is the creation of a tool for automated classification of craters preservation state on Mars Surface based on the state of its rim. A ternary method was implemented distinguishing the rim into three categories: Preserved, Modified and Degraded.

None of the few methods implemented until now follow this practice, so this project can be considered pioneer and useful for future investigations.

The results obtained in crater classification are good enough to be applied in crater images with certain characteristics. Images with some kind of superposition phenomena or affected by shadows due to the Sun position affect negatively the performance of the classifier. In the first case the algorithm actually extracts features that do not belong to the image being classified and in the second case shadows are perceived as texture features and also distort the learning phase of the Support Vector Machine Classifier.

The image resolution is also an important aspect, if we consider small images that are highly noisy it leads to the extraction of very few features that fail because of the redundancy of its information and also by the small number of samples that do not give enough information to be considered representative of a pattern of rim's behavior. Craters with radius dimensions bellow 16 pixels fit this category.

Images that do not exhibit this kind of behavior achieve satisfying classification results, the classifier was able to learn the tree types of rim. The occurred miss-classifications were easy explained because of the appearance of the rim in the modified category that in some cases presented similarities with the other two preservation stages.

Future improvements like combining more than one type of geological crater feature would be a possible approach to the construction of more reliable classifiers.

The application of methods that can detect and remove shadows and the subdivision of the crater into more sections so that the generalization in rims behavior decreases could also optimize the results.

As we know classifiers generally perform poorly on imbalanced datasets like happened in this study. A possible future improve would be using some approaches that could minimize the problem. The main reason for the SVM algorithm to be sensitive to class imbalance is that the soft margin assigns the same cost for both positive and

negative misclassifications in the penalty term. Using DEC (Different Error Cost) would cause the separating hyperplane to be skewed towards the minority class, which would finally yield a suboptimal model. Another approach that would make SVM less sensitive to outliers and noisy samples is a technique called Fuzzy SVMs.

Therefore, it made sense to apply these methods and compare the performances results.

Bibliography

- [1] Oakes, A. (2012). News Notes: Bluish flashes indicate daytime Saturn lightning; Curiosity lands on Mars for two-year mission; Young Belgian astronomer honoured as. *Journal of the Royal Astronomical Society of Canada*, 106, 187.
- [2] Bruckman, W., Ruiz, A., & Ramos, E. (2012). Earth and Mars crater size frequency distribution and impact rates: Theoretical and observational analysis. *arXiv preprint arXiv:1212.3273*.
- [3] Robbins, S. J., & Hynek, B. M. (2014). The secondary crater population of Mars. *Earth and Planetary Science Letters*, 400, 66-76.
- [4] W. A. Ambrose. First-Order Relationships Between Lunar Crater Morphology, Degree of Degradation, and Relative Age: The Crater Degradation Index, 2006
- [5] Hartmann, W. K., & Neukum, G. (2001). Cratering chronology and the evolution of Mars. In *Chronology and evolution of Mars* (pp. 165-194). Springer Netherlands.
- [6] Robbins, S. J., & Hynek, B. M. (2012). A new global database of Mars impact craters ≥ 1 km: 2. Global crater properties and regional variations of the simple-to-complex transition diameter. *Journal of Geophysical Research: Planets* (1991–2012), 117(E6).
- [7] Degirmenci, M., & Ashyralyyev, S. (2010). Impact crater detection on mars digital elevation and image model. *Middle East Technical University*.
- [8] Urbacha, Erik R., and Tomasz F. Stepinska. "Automatic detection of sub-kilometer craters in high resolution planetary images." *Preprint Submitted to Planetary and Space Science* 57.7 (2008): 880-887.
- [9] Bandeira, Lourenço, Jose Saraiva, and Pedro Pina. "Impact crater recognition on Mars based on a probability volume created by template matching." *Geoscience and Remote Sensing, IEEE Transactions on* 45.12 (2007): 4008-4015.
- [10] Yue, ZongYu, JianZhong Liu, and GanGuo Wu. "Automated detection of lunar craters based on object-oriented approach." *Chinese Science Bulletin* 53.23 (2008): 3699-3704.
- [10] V.Tamililakkiya, K.Vani, A.Lavanya and Anto Micheal. LINEAR AND NON-LINEAR FEATURE EXTRACTION ALGORITHMS FOR LUNAR IMAGES. *Signal & Image Processing: An International Journal (SIPIJ)*, December 2011. Vol.2, No.4.
- [11] Kamarudin, N. D., Ghani, K. A., Mustapha, M., Ismail, A., & Daud, N. G. N. (2014). An Overview of Crater Analyses, Tests and Various Methods of Crater Detection Algorithm. *Frontiers in Environmental Engineering*.
- [12] Wetzler, P. G., Honda, R., Enke, B., Merline, W. J., Chapman, C. R., & Burl, M. C. (2005, January). Learning to detect small impact craters. In *Application of Computer*

Vision, 2005. WACV/MOTIONS'05 Volume 1. Seventh IEEE Workshops on (Vol. 1, pp. 178-184). IEEE.

[13] Kim, J. R., Muller, J. P., van Gasselt, S., Morley, J. G., & Neukum, G. (2005). Automated crater detection, a new tool for Mars cartography and chronology. *Photogrammetric Engineering & Remote Sensing*, 71(10), 1205-1217.

[14] J.S. Marques, P.Pina, Craters delineation by Dynamic Programming. *IEEE Geoscience and Remote Sensing Letters*, 12(7): 1581-1585, 2015.

[15] Caetano, M. (2009). Image classification. *ESA Advanced Training Course on Land Remote Sensing, Prague (Czech Republic)*, 28.

[16] Halatci, I., Brooks, C., & Iagnemma, K. (2007, March). Terrain classification and classifier fusion for planetary exploration rovers. In *Aerospace Conference, 2007 IEEE* (pp. 1-11). IEEE.

[17] Godbole, Shantanu. "Inter-class relationships in text classification." (2006).

[18] Leger, P. C., Deen, R. G., & Bonitz, R. G. (2005, October). Remote image analysis for Mars Exploration Rover mobility and manipulation operations. In *Systems, Man and Cybernetics, 2005 IEEE International Conference on* (Vol. 1, pp. 917-922). IEEE.]

[19] Halatci, I., Brooks, C., & Iagnemma, K. (2007, March). Terrain classification and classifier fusion for planetary exploration rovers. In *Aerospace Conference, 2007 IEEE* (pp. 1-11). IEEE.

[20] Partio, M., Cramariuc, B., Gabbouj, M., & Visa, A. (2002, October). Rock texture retrieval using gray level co-occurrence matrix. In *Proc. of 5th Nordic Signal Processing Symposium* (Vol. 75).

[21] Dalal, N., & Triggs, B. (2005, June). Histograms of oriented gradients for human detection. In *Computer Vision and Pattern Recognition, 2005. CVPR 2005. IEEE Computer Society Conference on* (Vol. 1, pp. 886-893). IEEE.

[22] Lowe, D. G. (2004). Distinctive image features from scale-invariant keypoints. *International journal of computer vision*, 60(2), 91-110.

[23] Cristianini, N., & Shawe-Taylor, J. (2000). *An introduction to support vector machines and other kernel-based learning methods*. Cambridge university press.

[24] McEwen, A. S., Eliason, E. M., Bergstrom, J. W., Bridges, N. T., Hansen, C. J., Delamere, W. A., ... & Weitz, C. M. (2007). Mars reconnaissance orbiter's high resolution imaging science experiment (HiRISE). *Journal of Geophysical Research: Planets* (1991–2012), 112(E5).

[25]] K. Veropoulos, C. Campbell, and N. Cristianini, "Controlling the sensitivity of support vector machines," in *Proceedings of the International Joint Conference on Artificial Intelligence*, pp. 55–60, 1999.

[26] Pietikäinen, Matti, Topi Mäenpää, and Jaakko Viertola. "Optimizing color and texture features for real-time visual inspection." *Workshop on Texture Analysis in Machine Vision*. 2002.

Appendix A- Overall implementation of the SVM classifier

